Tests and measurements with a thermal VXD mock-up for BELLE II

Lars Hübner

geboren am: 29.03.1993

Matrikelnummer: 6322305

Bachelorarbeit in Physik
angefertigt am Deutschen Elektronen-Synchrotron DESY

vorgelegt der
Mathematisch-Naturwissenschaftlichen Fakultät
der
Universität Hamburg

Abgabe am: 13.03.2015

Hiermit bestätige ich, dass die vorliegende Arbeit von mir selbständig verfasst wurde und ich keine anderen als die angegebenen Hilfsmittel – insbesondere keine im Quellenverzeichnis nicht benannten Internet-Quellen – benutzt habe und die Arbeit von mir vorher nicht einem anderen Prüfungsverfahren eingereicht wurde. Die eingereichte schriftliche Fassung entspricht der auf dem elektronischen Speichermedium. Ich bin damit einverstanden, dass die Bachelorarbeit veröffentlicht wird.

Hamburg, ...
                       Datum   Unterschrift

1. Gutachterin: Prof. Dr. Caren Hagner
2. Gutachter: Dr. Carsten Niebuhr

Zusammenfassung

Im Zuge des Upgrades des Belle-Detektors am KEK in Tsukuba, Japan, wird ein CO_2-Kühlsystem integriert. Dieses wird aufgrund von neuen, stark temperaturempfindlichen Detektor-Komponenten benötigt. Insbesondere die dicht am Strahlrohr befindlichen PXD sind starken thermischen Belastungen ausgesetzt und müssen gekühlt werden. Darüber hinaus ist für die CDC eine konstante Temperatur nötig, um präzise Messungen durchführen zu können. Diese kann durch Hitzeentwicklung am SVD beeinflusst werden. Vor der Montage des Detektors sind daher Kenntnisse über die Wärmeerzeugung und -verteilung erforderlich. Zu diesem Zweck wird am DESY in Hamburg, Deutschland, ein Nachbau mit den innersten Detektormodulen konstruiert. Eine exakte Nachahmung des thermischen Verhaltens des Detektors soll damit möglich sein. Im Rahmen dieser Bachelorarbeit wurde die Kühlung des äußersten VXD Layer 6 in einem ebenen Aufbau untersucht. Der Schwerpunkt lag dabei auf der Hitzeentwicklung an den Sensoren, sowie Druckverlustmessungen der Kühlleitung. Es sollten Erkenntnisse darüber gewonnen werden, ob die anliegende Wärmelast abgeführt werden kann und wie hoch der Druckverlust über einer Leitung mit thermischer Last ist. Trotz Kühlung wurde ein starke Wärmeentwicklung festgestellt. Durch die ungünstige Lage der Thermistoren sind damit jedoch keine zuverlässigen quantitativen Aussagen über die vorherrschenden Temperaturen an den Sensordummies möglich. Der Druckverlust wurde ermittelt, ist jedoch durch große Unsicherheiten inakkurat. Weitere Messungen mit verbesserter Anordnung sind notwendig.

Abstract

As part of the Belle detector upgrade, located at the KEK in Tsukuba, Japan, a CO_2 cooling system will be added. Using new detector components, which are easily damageable or influenced by heat, make this step necessary. Particularly the next to the beam pipe located PXD is strained by high thermal load and therefore requires cooling. The CDC needs a constant temperature for precise measurements, but it could be influenced by heat from the SVD. Knowledge about the heat generation and distribution is needed before assembling the full detector. A mock-up of the innermost parts of the detector and a CO_2 cooling system is under construction at DESY in Hamburg, Germany, to gather such knowledge. The mock-up should be able to emulate the thermal properties of the final detector. Within the scope of this bachelor's thesis, the outermost VXD Layer 6 was studied in a flat arrangement. Focus lay on the heat dissipation at the sensors and on pressure drop measurements of the cooling pipe. It was investigated whether the applied heat load can be sufficiently lead away and how large the pressure drop is along the experiment line. Despite cooling was applied, a remarkable rise in temperature was observed. However, the unfavorable position of the thermistors make reliable quantitative statements of the sensor dummies' temperatures impossible. The pressure drop was determined, but is of limited accuracy due to large uncertainties. Further investigations have to be made with a better set-up.

Contents

Introduction

In the past decades many physical theories could be tested and validated by the help of particle physics. As a part of this process the Belle experiment at Kō Enerugī Kasokuki Kenkyū Kikō (KEK) in Tsukuba, Japan, analyzed the flavor structure of fundamental particles leading to the confirmation of the *CP* violation in the quark sector predicted by the Standard Model (SM). Nevertheless there are still unresolved problems in the SM, which makes searching for new physics worthwhile. An upgrade of the Belle experiment, Belle II, aims to answer some of the open questions with high precision measurements. During the upgrade new components will be used. Due to expected heat generation by the read-out electronics, a two-phase cooling system, using CO_2 as coolant, will be installed. Two-phase cooling with CO_2 allows for high cooling performance at low material budget, which is important to not reduce precision of measurements, i.e. by multiple scattering. Using a phase transition from liquid to gas state in addition to convective cooling makes this superior to single-phase cooling, as it's own temperature does not increase on heat intake. This is desired for accurate measurements of the CDC, which might be influenced by the SVD. Validation of the ability to reach the necessary cooling performance using this concept is required. Previous simulations and experiments analyzed only single components [A+10], but the thermal behavior of a more complete model is needed. Therefore a mock-up for thermal studies is currently under construction at Deutsches Elektonen-Synchrotron (DESY) in Hamburg, Germany. It should be able to realistically emulate the heat generation at the innermost detector parts, including mainly vertex detectors (VXD), of the upcoming Belle II experiment.

As a part of this bachelor's thesis the VXD Layer 6 of the thermal mock-up was assembled in a flat arrangement with an external CO_2 cooling system connected. Heaters on the ladders simulated heat dissipation like expected for the real read-out chips. Thermal properties of the VXD Layer 6, while using two-phase cooling, were tested in this configuration. The main focus during these tests is on the pressure drop along the tube and the heaters' temperatures at different mass-flow rates, coolant temperatures and amount of power applied. Furthermore it was investigated how to indicate whether the CO_2 is in two-phase or liquid state, and how to determine if dry-out occurs.

This thesis is structured as follows. Chapter 2 gives an overview about the Belle II detector. The main focus is on the components used in the thermal mock-up. In chapter 3 the basic principles of the occuring thermodynamic processes are descibed. The experimental setup and the cooling system are explained in chapter 4. This is followed by the experimental results achieved using the mock-up in chapter 5. Finally, a conclusion is drawn from the previously presented results in chapter 6.

BELLE II At SuperKEKB

The Belle experiment operated from 1999 to 2010 and collected a integrated luminosity of over $1\,\text{ab}^{-1}$ at the asymmetric KEKB collider at KEK. While mainly analyzing *B* decays, it contributed to topics such as *CP* violation, mixing, rare decays, and many others. Both, detector and collider, will be upgraded, to Belle II and SuperKEKB repectively. Higher statistics will be achieved, while being sensitive to effects from New Physics in rare and higher order processes [A+10]. This opens the opportunity to probe the SM to an unprecedented precision. Physics run is intended to start in early 2018 with Belle II's goal to collect a integrated luminosity of $50\,\text{ab}^{-1}$ by 2025.

This chapter gives a brief overview on the SuperKEKB collider and the Belle II detector. The VXD, composed of 2 layers of pixel detectors (PXD) and 4 layers of silicon vertex detectors (SVD), and representing the innermost detector parts, will be discussed in more detail and cooling concepts for both presented.

2.1 SuperKEKB collider

The asymmetric SuperKEKB electron-positron collider is the successor of the 1998 to 2010 operational KEKB. It is currently under construction at KEK. A schematic drawing is shown in Fig. 2.1, with the Belle II detector on the top right.

The instantaneous luminosity will be increased by a factor of 40 to $80 \times 10^{34}\,\text{cm}^{-1}\text{s}^{-1}$ compared to KEKB, which provided $2.11 \times 10^{34}\,\text{cm}^{-1}\text{s}^{-1}$. The luminosity is approximately given by [A+10] as

$$L \approx \frac{\gamma_{\pm}}{2er_{\text{e}}} \left(\frac{I_{\pm}\xi_{y\pm}}{\beta^*_{y\pm}} \right) \tag{2.1}$$

where γ is the Lorentz factor, e the elementary electrical charge, and r_{e} the electron classical Radius. The suffix $\pm$ denotes the electron (-) or positron (+) beam. To reach the desired luminosity, the vertical beta function (β^*_y) will be reduced and the beam current I increased. SuperKEKB will mainly run at a center of mass Energy of $E_{CMS} = 10.58\,\text{GeV}$, hitting the $\Upsilon(4S)$ resonance, which is expected to decay primarily ($> 96\%$) into $B\bar{B}$ [Oli+14]. To counteract growing emittance and decreasing beam lifetime, the beam asymmetry will be reduced. During the update, also the collision angle ϕ will be increased. See Table 2.1 for a comparison of KEKB and SuperKEKB parameters.
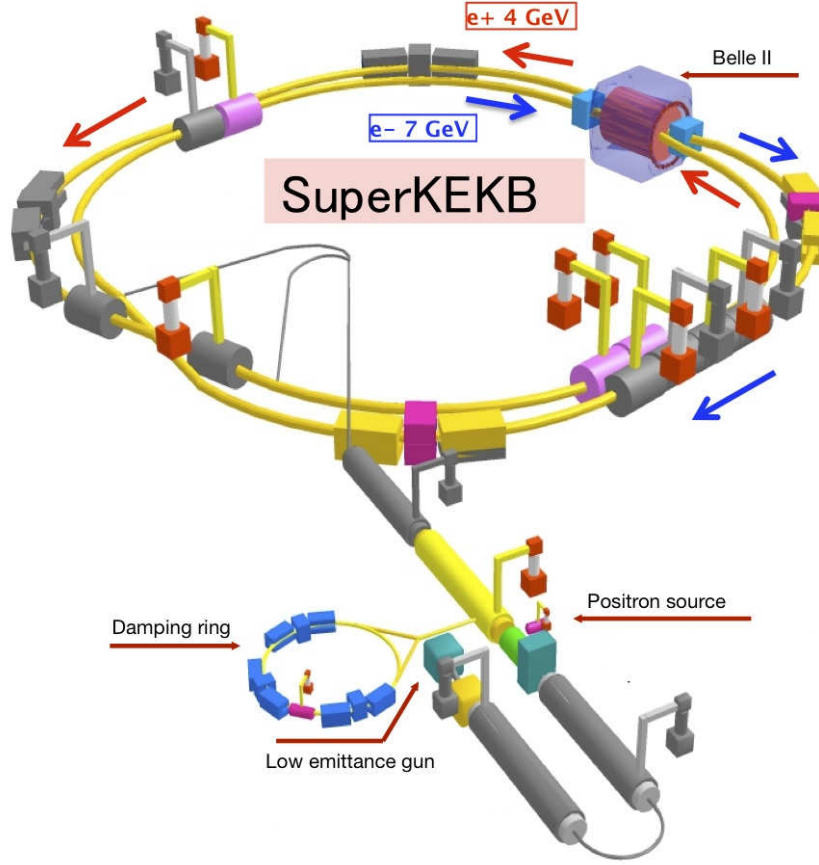
Figure 2.1: Schematic drawing of the SuperKEKB collider. [B+12]

Table 2.1: Comparison of KEKB and SuperKEKB parameters. If two values: LER(e$^+$) / HER(e$^-$). [A+10; HIG]

	KEKB	SuperKEKB	
Energy	3.5/8.0	4.0/7.0	GeV
ξ_y	0.0028/0.0881	0.0012/0.0807	
β_y^*	5.9/5.9	0.27/0.3	mm
I	1.64/1.19	3.6/2.6	A
ϕ	22	83	mrad
L	2.11	80	$10^{34}\,\mathrm{cm}^{-1}\mathrm{s}^{-1}$

2.2 Belle II Detector

As side-effect of the increased luminosity there will also be higher background. A rise of factors of 50 and 20 are expected for physics event rate and background hit rate respectively. One has to cope with higher occupancies and radiation doses. For this purpose redesigns of several detector components were made that maintain or improve Belle's performance. A model of the Belle II detector is shown in Fig. 2.2.
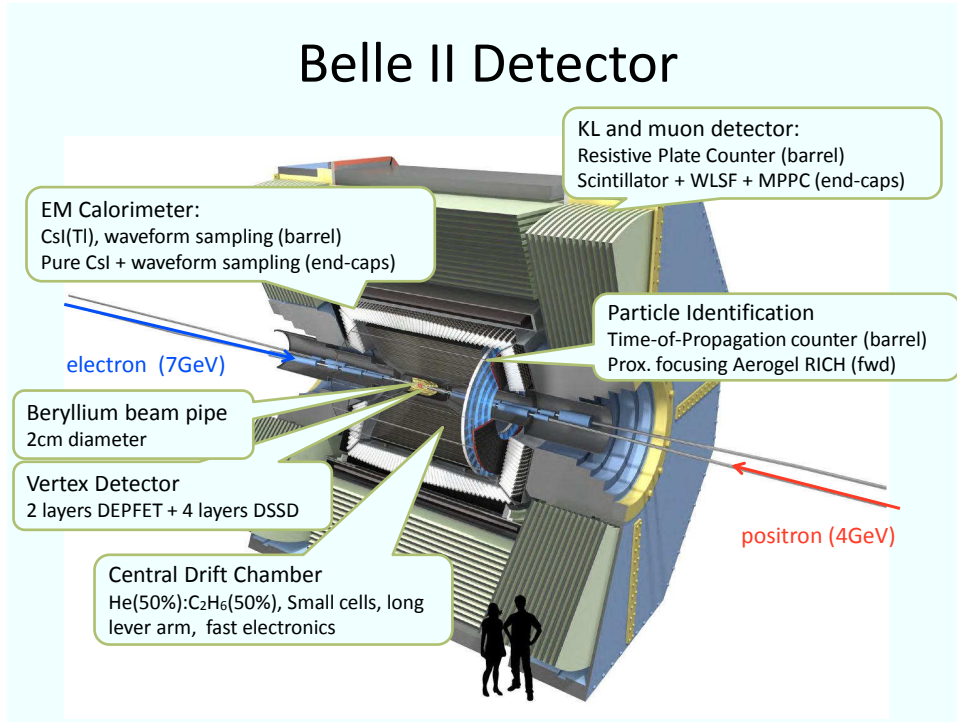

Figure 2.2: Schematic drawing of the Belle II detector. [B+12]

It's parts are arranged in an "onion-like" shape. The beam pipe at the interaction point is a double walled Beryllium pipe with 10 mm inner and 12 mm outer radius. Close to the beam pipe two PXD layers were added, followed by four SVD layers, together forming the VXD. For the layers' ladder and sensor counts, and their radii, see Table 2.2. The Layers are numbered from 1 to 6 from the innermost to the outermost. The VXD is surrounded by a central drift chamber (CDC), particle identification system (PID) and electromagnetic calorimeter (ECL). These components are encapsulated by a superconducting solenoid coil. The outermost part is the K-Long/Muon detector (KLM) covered by an iron yoke. The VXD will be operated in a cold dry volume with the Temperature above it's dew point.

2.2.1 Pixel Detector (PXD)

Due to the higher luminosity in SuperKEKB, the occupancy would not allow for vertex reconstruction anymore, if using strip detectors. Therefore the SVD is moved away from the beam pipe and two layers of pixelated silicon sensors are added in between. To avoid multiple scattering thin layers are required, which are made possible by the DEPFET (DEPleted Field Effect Transistor) technology. A thickness of 75 μm can be obtained, because the position of the read-out electronics lies out of the acceptance area. A model of the PXD mounted on the beam pipe can be found in Fig. 2.3.

Table 2.2: Counts of the VXD layer's ladders and sensors per ladder

Layer	Type	Radius [mm]	# Ladders	# Sensors/Ladder	# Sensors Total
1	PXD	14	8	2	16
2	PXD	22	12	2	24
3	SVD	38	7	2	14
4	SVD	80	10	3	30
5	SVD	104	14	4	56
6	SVD	135	16	5	80
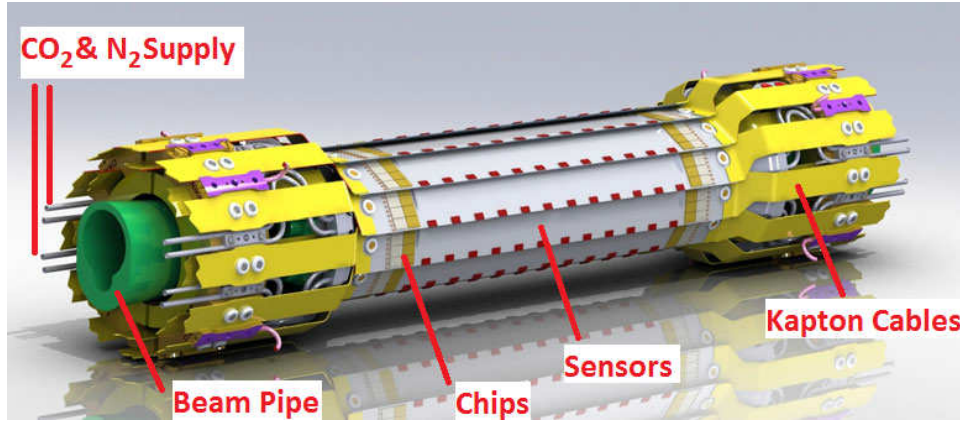
Figure 2.3: PXD mounted on beam pipe. [Gfa12]

The sensors themselves have a heat generation of about 1 W each over their whole surface. Most heat production occurs at the read-out chips, which contribute 8 W per sensor. This yields to a thermal power of 18 W per ladder or 360 W for the whole PXD. To avoid damage the temperatures must not exceed 60 °C for the sensors and 30 °C for the read-out chips. Despite air cooling being sufficient for the sensors, the read-out chips must be actively cooled. Two-phase cooling, using CO_2 at $\lesssim -20$ °C as a coolant, is believed to have this performance. The sensors will be cooled by a Nitrogen flow at speed of $1\,^m/_s$ and a temperature of 0 °C. The supporting structure, which will be used to mount the PXD to the beam line, contains channels for N_2 and CO_2. Thus this "Support and Cooling Block" (SCB) will act as a heat sink. A schematic design and a photo of the SCB are shown in Fig. 2.4(a) and (b). Four SCB, two for upper and lower hemisphere respectively, are needed.

2.2.2 Silicon Vertex Detector (SVD)

As opposed to the PXD, the SVD consists of double-sided silicon strip detectors (DSSD) to have a lower channel amount, and to reduce material and costs. Reconstruction precision of Belle's SVD should be maintained or improved. The upgraded SVD has to cover the whole polar angular acceptance of $17° < \Theta < 150°$ at a greater distance to the interaction point than in Belle. The cylindrical design is replaced with an asymmetrical lantern shape to achieve that. Slanted sensors with trapezoidal shape are added in the forward region for the Layers 4 to 6. Fig. 2.5 shows two models of the SVD with the different sensor shapes. All ladders will be mounted on endrings, which are composed from 2 halves each, similiar to the SCB. Layer 3 and 4 share their endrings. Photos of endring-halves as of the current design and fabrication process are shown in Fig. 2.6.
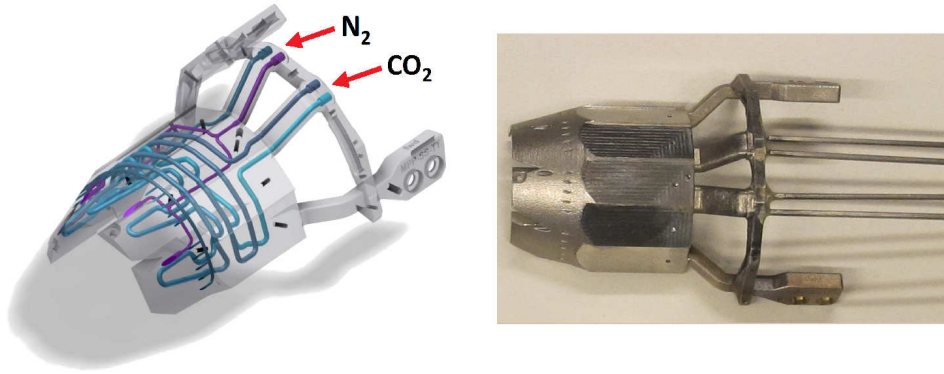
Figure 2.4: Support and Cooling Block.
(a) Left side - Schematic design of SCB. Purple and green channels for N_2, dark and light Blue channels for CO_2. [Nie14], design by MPI.
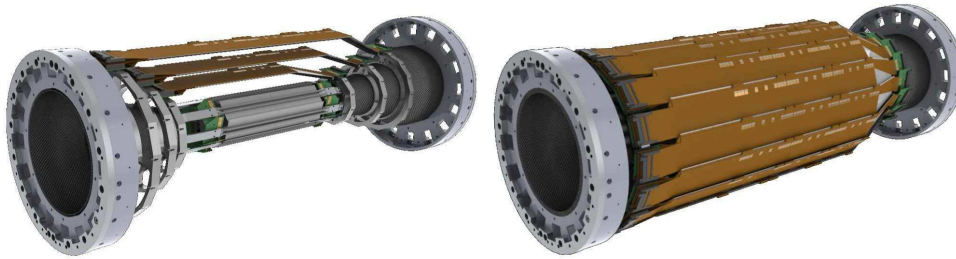(b) Right side - Photo of 3D-printed SCB made of stainless steel

Figure 2.5: SVD Layout with sensor shapes. Left side: Full layer 3 and one ladder for layers 4-6 each. Right Side: Full SVD. [Fra13]
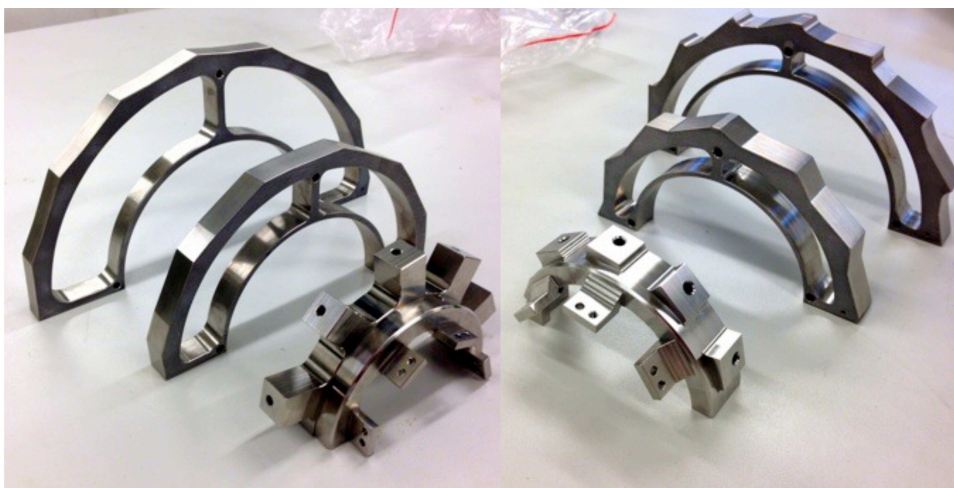

Figure 2.6: SVD endrings as of the current design and fabrication process.

In principle the SVD is operational without cooling, but thermal waste has to be transported out of the SVD volume. It's outside temperature must be 23 °C, because the CDC measurements require an precise and constant ambient temperature. Also tests show a better signal to noise ratio when cooled [Gfa12]. The thermal power generated by the SVD is about 666 W, of which 328 W are caused by the center sensors' read-out chips and 338 W by the ones on the edges. The endrings provide cooling channels for the read-out chips similar to the SCB, also using CO_2 as coolant. However, the used read-out chips (APV25) have to be as close to the sensors as possible and therefore placed onto the sensor. Cooling through the endrings is only applicable for the outer sensors of each ladder. For the other sensors, "origami cooling" will be used, where cooling pipes are directly attached to them. To keep the material budget low, small tube diameters are needed. Low mass flow rates of the coolant are desired to keep the pressure drop low, caused by fluid friction inside of the tubes. A pressure drop causes a temperature drop, which should be avoided. CO_2 at $\lesssim -20$ °C should be able to fulfill these requirements. Fig. 2.7 shows a model of a SVD dummy sensor including a stainless steel cooling tube with outer diameter of 1.6 mm attached to it.

For this thesis a naming scheme for the sensors will be used to avoid confusion. The pattern is "Layer.Ladder.Sensor" as shown in Fig. 2.8. The ladder numbers are applied counter-clockwise. I.e. L6.1.1 refers to the first sensor of ladder 1 in layer 6.
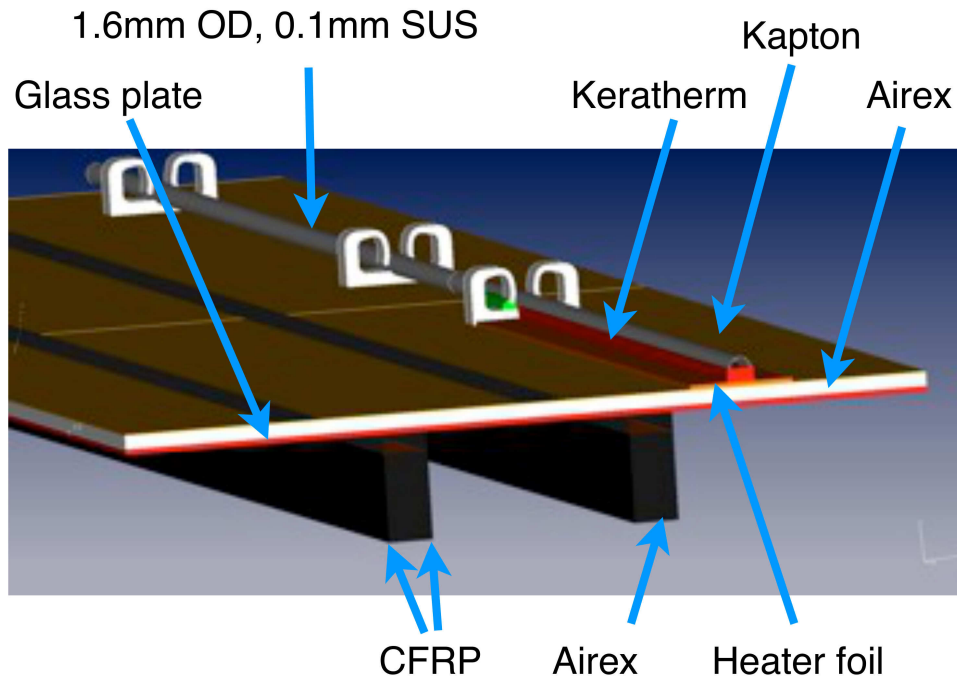

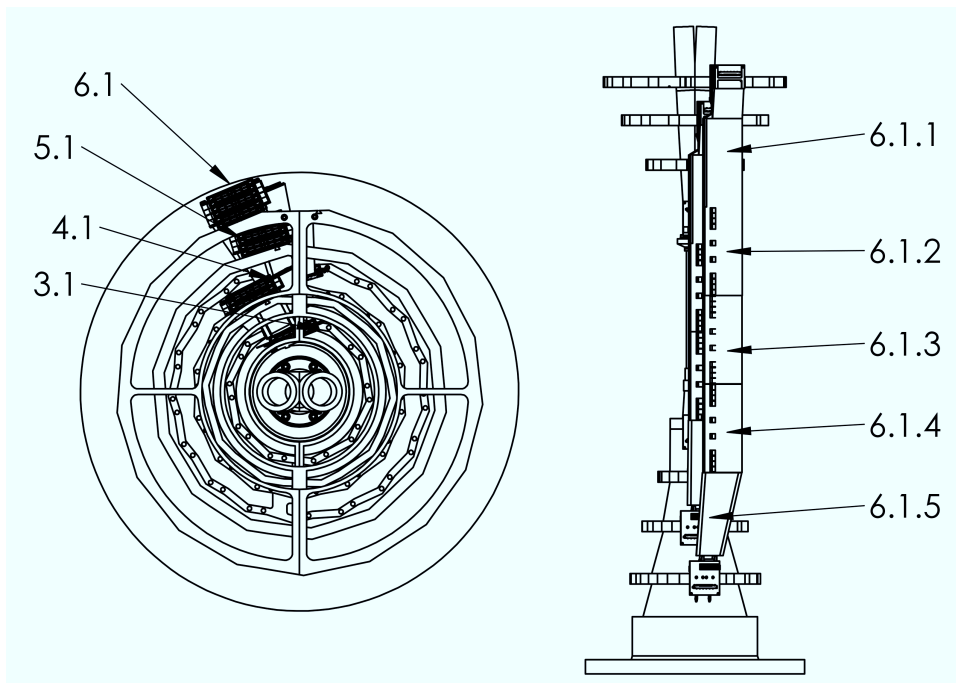Figure 2.7: SVD dummy Sensor with cooling pipe attached. [Nie14]

Figure 2.8: VXD naming scheme. [M+12]

Theory

This chapter is intended to convey the basic principles the experiment is based on. This covers information on the two-phase state, it's usage for evaporative cooling, boiling and flow patterns in tubes, different types of heat transfer and pressure drop effects in tubes.

3.1 Two-Phase State

The state of a thermodynamic system can be described by parameters, such as pressure P, temperature T, volume V, entropy S, chemical potential μ and number of particles N. A set of states with uniform, homogeneous physical properties is called a phase. Using the above parameters one can find thermodynamic potentials, which fully represent a state. One of these is the Gibbs Energy G. It is given by

$$G = H - S \cdot T \tag{3.1}$$
$$= U + P \cdot V - S \cdot T \tag{3.2}$$

where the Inner Energy U and the Enthalpy H are also thermodynamic potentials. In it's differential form it can be expressed as

$$\mathrm{d}G = -S\,\mathrm{d}T + V\mathrm{d}P + \sum_i \mu_i \mathrm{d}N_i \tag{3.3}$$

with i chemical components. For an equilibrium state the Gibbs Energy is minimal, hence $\mathrm{d}G = 0$, and does not change $\Delta G = 0$. According to Gibb's Phase Rule, the degrees of freedom F, for a thermodynamic system to be in an equilibrium state, are given by

$$F = C - \Pi + 2 \tag{3.4}$$

with the number of chemical compounds C and coexistent phases Π. For a pure substance ($C = 1$) in a single phase ($\Pi = 1$) one can choose two variables, i.e. pressure and temperature, independently and still find an equilibrium, if they lie in the phases boundaries. To find three phases ($\Pi = 3$) simultaneously, all variables have to be fixed, meaning, that it can only exist at a single point. For a mixture of vapor, liquid and solid phase this is called "triple point". When trying to find equilibrium in a two-phase state ($\Pi = 2$), only one variable can be set freely. A change in temperature must cause a change in pressure and vice versa, leading to a phase boundary line.

For the mentioned equilibrium conditions to hold in two-phase state, both phases need to have same Gibbs Energy $G_1 = G_2$ and therefore chemical potential $\mu_1 = \mu_2$. For a given temperature or pressure a

phase transition then can occur by a change in enthalpy, entropy and volume.

Fig. 3.1 shows a pressure-enthalpy phase diagram for the transition from liquid to vapor state for CO_2. The shape of the parabola can be obtained by solving the equation of state, i.e. Van-der-Waals Equation or Dieterici Equation. Isotherms under the parabola are given by Maxwell's Equal Area Rule and are identical to the isobars. The vapor quality $x \in [0, 1]$ describes the fraction of the system in liquid ($x = 0$) and vapor state ($x = 1$).

The change in enthalpy is given by

$$\mathrm{d}H = \delta Q + V\mathrm{d}P - \delta W' \tag{3.5}$$

where δQ is the amount of heat added to the system and $\delta W'$ the performed work (without expansion). If the pressure is kept constant and $\delta W' = 0$, then

$$\mathrm{d}H = \delta Q. \tag{3.6}$$

This principle is used during the cooling of the VXD Layer 6. However, small changes in pressure are expected, causing a change in temperature as well.
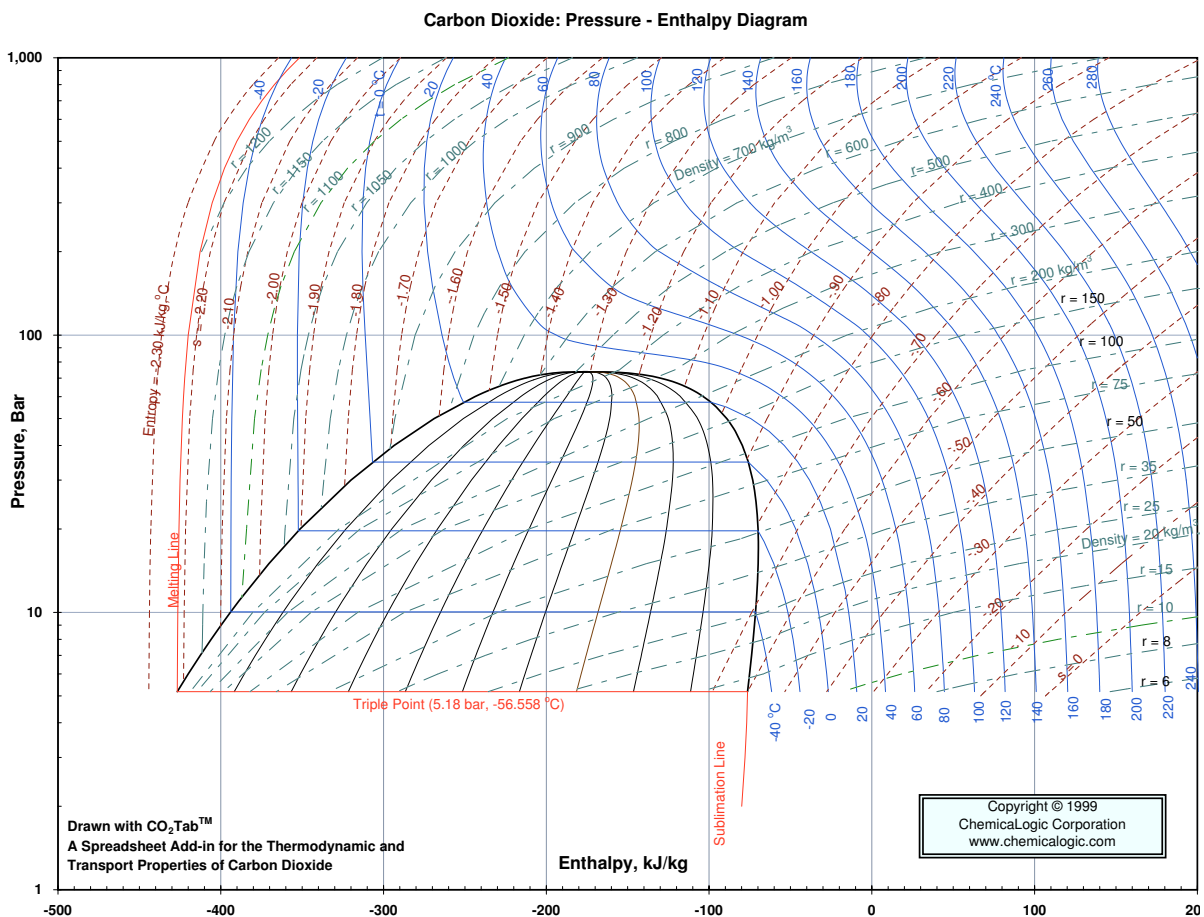
Figure 3.1: CO_2 P-H phase diagram. Shown are isotherms (blue lines, in °C), enthropy (dashed red lines, in $\mathrm{kJ\,kg^{-1}\,°C}$), density (dashed green lines, in $\mathrm{kg/m^3}$), phase transition to solid state (red lines), and the vapor quality in the liquid-vapor equilibrium (black lines, in 0.1 steps). [Che99]

3.2 Heat Transfer

This section presents some formulas to calculate heat transfer, especially in and through cylindrical geometries, such as (concentric) tubes.

3.2.1 Solid Body

As a foundation for heat transfer calculations one uses Fourier's Law

$$\dot{\vec{q}} = -\lambda \vec{\nabla} T \tag{3.7}$$

where $\dot{\vec{q}}$ is the local heat flux density and λ the material's conductivity. The heat flux $\dot{Q}$ can be achieved by integrating over the material's surface S:

$$\dot{Q} = \oint_S \dot{\vec{q}} \mathrm{d}\vec{A} \tag{3.8}$$

These formulas are valid if the thermal conductivity is identical in all directions, i.e. homogeneous materials. For a cylindrical tube it simplifies to

$$\dot{q} = -\lambda_\text{tube} \, \frac{\mathrm{d}T}{\mathrm{d}r} \tag{3.9}$$

$$\dot{Q} = -2\pi r L \, \lambda_\text{tube} \, \frac{\mathrm{d}T}{\mathrm{d}r} \tag{3.10}$$

with a radial position r and the tubes length L. This can be solved to

$$\dot{Q} = \lambda_\text{tube} \, 2\pi L \, \frac{\Delta T}{\ln(r_o/r_i)} \tag{3.11}$$

where the indices i and o denoting the inner and outer tube. Typically the temperatures of the tube's inner and outer surface are unknown, but those of the surroundings. In that case one has to take into account a heat resistance R, describing the amount of heat transferred between the tube's walls and these surroundings. In case of fluids or dense gases, with the temperature difference ΔT at the inside and outside of the tube, the heat flux can then be calculated by

$$\dot{Q} = \frac{\Delta T}{R} \tag{3.12}$$

with

$$R = \frac{1}{2\pi L} \left(\frac{1}{\alpha_i r_i} + \frac{1}{\alpha_o r_o} + \frac{1}{\lambda_\text{tube} \, \ln(\frac{r_o}{r_i})} \right) \tag{3.13}$$

where $\alpha_{i/o}$ is the heat transfer coefficient between the tube and what's inside and outside of it.

3.2.2 Gas

In case of dense or moderately thinned, resting gases eqn. 3.7 holds. In the former case, it yields the same results as for a solid body. In the latter case, there might be jumps in temperature at the tube walls, which can be added to the formulas by additional boundary conditions. A solution for the heat flux through moderately thinned gases $\dot{Q}_{\mathrm{mtg}}$ between concentric cylinders is given in [Ver13] for gases below a Knudsen Number $Kn \lesssim 0.1$ as

$$\dot{Q}_{\mathrm{mtg}} = \dot{Q}_{\mathrm{kont}} \frac{\ln{(r_2/r_1)}}{\ln{(r_2/r_1)} + (15/8)(1 + r_1/r_2)Kn} \tag{3.14}$$

where the continuum heat flux is given by $\dot{Q}_{\mathrm{kont}} = \dot{Q}/r_1$ from eqn. 3.12.

For higher Knudsen Numbers a more reliable solution was given by Lees and Liu [LL62] as

$$\dot{Q}_{\mathrm{tg}} = \dot{Q}_{\mathrm{kont}} \left(1 + \frac{15}{4\gamma_1} \frac{f \cdot Kn}{ln\,(r_2/r_1)}\right)^{-1} \tag{3.15}$$

with the accommodation coefficient γ_1 for the interaction between the gas and the surface of the inner cylinder. f is a correction factor for polyatomic gases.

In the case of air ($f \simeq 0.67$) at low pressures with the inner tube being made of copper ($\gamma_1 \simeq 1$) eqn. 3.15 can be approximated by

$$\dot{Q}_{\mathrm{tg}} \simeq \dot{Q}_{\mathrm{kont}} \left(1 + \frac{1}{4P} \frac{1}{ln\,(r_2/r_1)}\right)^{-1} \tag{3.16}$$

3.2.3 Radiation

Every body with a temperature $T > 0\,\mathrm{K}$ emits electromagnetic radiation of a specific spectrum of wavelengths. In the simplest model, that of a black body, this spectrum solely depends on the body's temperature. The energy flux per surface element is given by the Stefan-Boltzman-Law as

$$\dot{e} = \sigma T^4 \tag{3.17}$$

where σ is the Stefan-Boltzmann constant. For a more realistic model a emission coefficient $0 \le \epsilon < 1$ is added to describe the influence of the material and it's surface

$$\dot{e} = \epsilon \sigma T^4 \tag{3.18}$$

The total radiative heat flux from one object to another yields from this equation, when one takes into account how the surfaces are oriented to each other and how much radiation is absorbed, reflected or transmitted. For arbitrary surfaces view factors $\phi_{i,j}$ have to be calculated, which are defined as the quotient of energy transmitted from surface i to j to the total energy emitted by surface i.

For a concentric tube the heat transferred by radiation from the inner to the outer tube is given by

$$\dot{Q}_{\mathrm{rad,i} \rightarrow \mathrm{o}} = \frac{\sigma(T_i^4 - T_o^4)}{\frac{1}{\epsilon_i A_i} + \frac{1}{\epsilon_o A_o} + \frac{1}{A_i}} \tag{3.19}$$

3.3 Boiling And Two-Phase-Flow

When a liquid in a tube is heated until it reaches it's boiling point for a given pressure, then boiling occurs. Depending on the boiling mode there are different heat fluxes. At low heat fluxes, small bubbles form at nucleation sites on the tube's surface, which is called nucleate boiling. If the heat flux is above a critical value, the complete surface will get covered in vapor. This mode is called film boiling. Since there is no liquid on the tube walls anymore, one also speaks of dry-out. The vapor-film is less capable of carrying heat away and therefore the tube's temperature rises. Thus if used for cooling purposes, dry-out should occur.

Inside a tube with forced convection both, nucleate and film boiling, can be present at the same time, due to turbulences in the flow. The vapor-liquid ratio influences which mechanism is predominantly, where a higher amount of vapor encourages film boiling. The two-phase flow, composited of vapor and liquid, and it's properties, can be described by models from Friedel [Fri79] and Thome [Tho+08; TCR08]. In Friedel's model, the mixture's differences to a single-phase fluid are handled by a two-phase multiplier ϕ, which is derived from Friedel's Correlation. In this case the heat transfer coefficient α_i in eqn. 3.12 is calculated by the Dittus-Boelter Equation for turbulent flow

$$\alpha_i = \frac{\lambda_{\text{fluid}}}{d_i} \left(0.023 Re^{0.8} Pr^{0.4} \right) \tag{3.20}$$

with the Prantl Number Pr. Since the Reynolds Number ($Re = \frac{\dot{m}d_i}{\nu}$, with viscosity ν) is proportional to the mass flow, a better heat transfer is expected at higher flow rates.

Despite to this, Thome's model uses flow patterns, depending on the vapor quality, using different calculation methods. Fig. 3.2 shows these flow patterns for evaporization in horizontal tubes. The heat transfer coefficient is given by

$$\alpha_i = \frac{\Theta_{\text{dry}}\alpha_v + (2\pi - \Theta_{\text{dry}})\alpha_{\text{wet}}}{2\pi} \tag{3.21}$$

where Θ_{dry} is the angle of the tube being dry, α_v and α_{wet} the heat transfer coefficient of the vapor and liquid part to the tube, respectively. These parameters are functions of the individual state. Qualitatively an increase in vapor quality x leads to a slight increase of α_i until dry-out occurs at $x \approx 0.6 \ldots 0.8$.
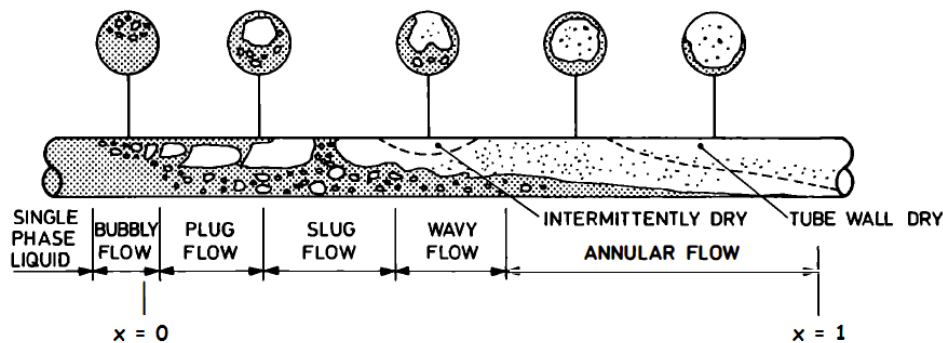

Figure 3.2: Flow patterns according to Thome with vapor quality x. [Tho06]

3.4 Pressure Drop In Tubes

The total pressure drop is the sum of the gravitational pressure drop ΔP_g, the momentum pressure drop ΔP_m and the frictional pressure drop ΔP_f:

$$\Delta P = \Delta P_g + \Delta P_m + \Delta P_f \tag{3.22}$$

The first part can be calculated by

$$\Delta P_g = \rho_H \, g \, \Delta h \, \sin(\Theta) \tag{3.23}$$

with gravitational constant g, vertical height difference Δh, angle with respect to the horizontal Θ and the homogeneous density ρ_H. The latter one can be calculated from the densities of the vapor ρ_v and liquid ρ_L parts. For further information, see [Tho06].

The momentum pressure drop, reflecting the change in kinetic energy of the flow, is given by

$$\Delta P_m = \dot{m}^2 \left(\left[\frac{(1-x)^2}{\rho_L(1-\epsilon)} + \frac{x^2}{\rho_v \epsilon} \right]_{\text{out}} - \left[\frac{(1-x)^2}{\rho_L(1-\epsilon)} + \frac{x^2}{\rho_v \epsilon} \right]_{\text{in}} \right) \tag{3.24}$$

where the void fraction ϵ is a function of x, $\dot{m}$, ρ_L and ρ_v.

The methods of calculating the frictional pressure drop of a two-phase flow differ in the Friedel Model and the Thome Model. As mentioned before, in the former one it is obtained by a two-phase multiplier, thus

$$\Delta P_f = \phi^2 \Delta P_L \tag{3.25}$$

with the frictional pressure drop caused by a single-phase liquid ΔP_L. This can be calculated using the Darcy-Weißbach Equation. For the Thome Model it has to be calculated differently for every flow pattern. A complete list with calculations can be found in [Tho+08]. For further pressure drop effects, see i.e. [Ver13].

Experimental Setup

As part of the thermal studies for the innermost detectors of BELLE II an experiment is set up in the HERA WEST hall at DESY in Hamburg. This experiment is intended to emulate the thermal behavior of the VXD Layer 6 in a simplified manner. In this chapter the experimental setup, consisting of the CO_2 supply system MARCO, the VXD Layer 6 arrangement and the concentric tubes (Flex Lines) connecting both, are described.

4.1 MARCO

As supplier for the coolant a Multipurpose Apparatus for Research on CO_2 (MARCO) is used. It is a 2-Phase Accumulator Controlled Loop (2-PACL) device, which can supply CO_2 with temperatures of $-40\,°C$ to $25\,°C$ [Ver11b]. A model of MARCO is shown in Fig. 4.1. One can see the accumulator which controls the pressure and therefore the saturation temperature where the CO_2's phase-transition from liquid to gas occurs. The CO_2 in the accumulator is cooled by a chiller, located underneath MARCO's CO_2-loop (not shown in the pictures). The liquid pumps usually can deliver the cooled CO_2 at mass flow rates of $5\,^g/_s$ to $30\,^g/_s$. By manually overriding the automatic pump speed control one is able to reduce the mass flow below the limit of $5\,^g/_s$. MARCO comes with it's own computer system to control all components, but also supports the connection of an external computer. The latter is the preferred method, which is also in this setup.
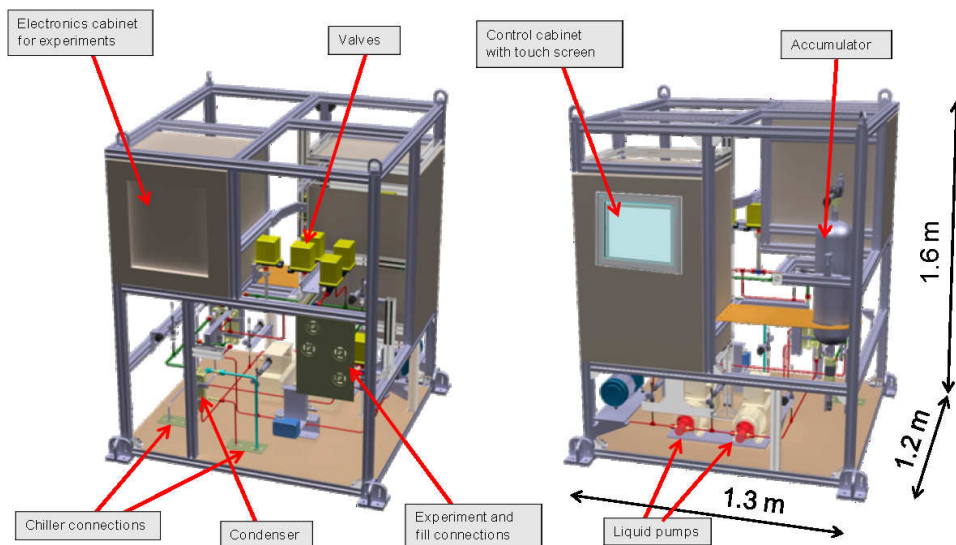
Figure 4.1: Model of MARCO showing the location of main components. [Ver11a]

A more detailed view is given by MARCO's schematic design shown in Fig. 4.2, with the experiment loop on the left side and the chiller loop on the right side (blue). To control the CO_2's pressure the Accumulator (AC119) is equipped with an electric heater (HT119) and a cooling loop from the chiller (HX119/HX212). After leaving the accumulator the CO_2 has to be cooled by a heat exchanger connected to the chiller (HX101/HX208) to ensure that it is in liquid state. Otherwise the pumps (PM101/PM102) could be damaged. The pumps deliver the desired mass flow which can be measured with a flowmeter (FT103). Additionally they increase the pressure which is measured (PT103). To achieve the desired temperature in front of the experiment (TT105) another heat exchanger (HX104/HX118) provides heat build-up by the return flow. The pressure drop over the experiment can be measured with two sensors in front of the heat exchanger (PT104) and in MARCO's CO_2 inlet from the experiment (PT118). Due to the design the pressure at the return is equal to the one set by the accumulator. Not shown in this schematics, but controllable by MARCO, is an additional electrical heater set between the experiment and the inlet. It can be used to increase the return flow's temperature to influence and stabilize the CO_2 temperature towards the experiment.
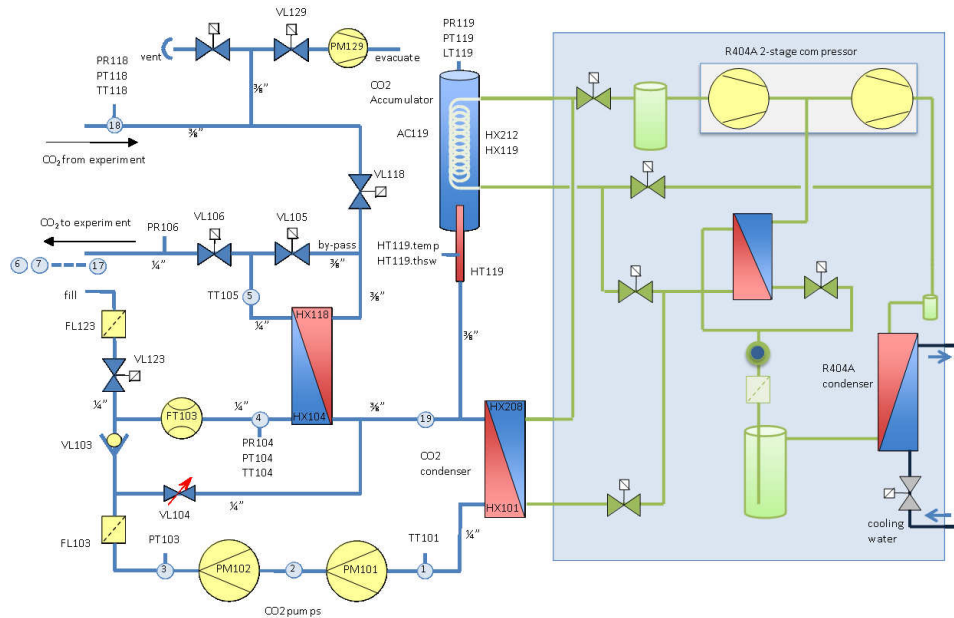
Figure 4.2: Schematic design of MARCO. [Ver11a]

MARCO has some features to avoid damaging components. To always have enough liquid at the pumps, even at low mass flow rates, there is a valve bypassing the experiment (VL104). If the pressure drop dP103 = PT103 − PT118 is greater than 10 bar for a certain time, the pumps are shut down. For the experiments made, this yields to an upper limit for the mass flow of 7.5 $^g/_s$ to 8.5 $^g/_s$.

4.2 Flex Lines

The connection between MARCO and the experiment is done via concentric tubes called Flex Lines. A schematic design of the Flex Lines is shown in Fig. 4.3. Dimensions can be found in Table 4.1. The inner tube is used as the experiment's CO_2 supply line, while the outer tube returns it back to MARCO. This design was chosen to have the highest pressure drop, caused by the small diameter, in front of the experiment, which is important to achieve two-phase. Additionally the outer tube acts as an heat

insulation for the inner tube against the outside. To further decrease heat transfer between the tubes and the outside, the tubes are placed inside a corrugated stainless steel (SST) hose with an insulating vacuum in between them provided by a turbo pump.
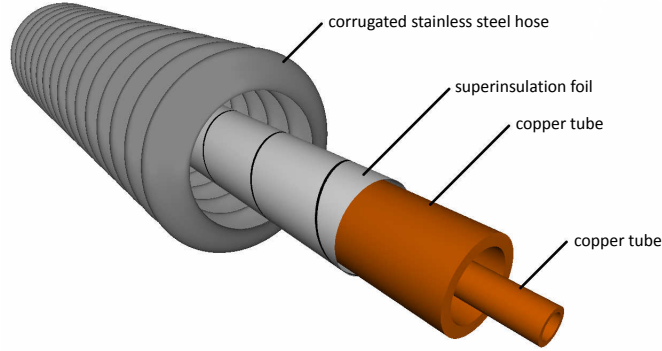
Figure 4.3: Schematic design of Flex Lines.

Table 4.1: Dimensions of Flex Lines

Length L		8 m	
Inner tube diameters $d_{1,inner}/d_{1,outer}$	1 mm	/	1.6 mm
Outer tube diameters $d_{2,inner}/d_{2,outer}$	3 mm	/	4 mm
SST hose diameters $d_{SST,inner}/d_{SST,outer}$	8 mm	/	12 mm
Gas pressure $P_{SST-2,outer}$		$<1 \times 10^{-5}$ bar	

A calculation for the heat transfer caused by radiation, based on the equations for gray body radiation (eqn. 3.19) and gases at low pressures (eqn. 3.16), was made and is shown in Fig. 4.4. Although being only an approximation for an ideal, straight concentric tube with same radial distances, no bends, and no touching of the tubes, this suggests the reduction of radiative heat transfer at low pressures through superinsulation as an effective method. Therefore the outer CO_2 tube is encased with superinsulating foil. According to [Ver13], the ideal number density N/D of the foils is about $20\,\mathrm{cm}^{-1}$ to $30\,\mathrm{cm}^{-1}$, while a little amount of space between the layers result in better insulation performance. This consideration led to an about 3-ply wound of the foil around the tube to get an insulation thickness of $\leqslant 1$ mm.

In this experiment six Flex Lines are connected through a distributor to MARCO. Every tube has a valve which can be used to interrupt the flow on single lines. One Flex Line is connected to the VXD Layer 6 and four are connected to bypasses, to get a lower massflow in the experiment line. A spare Flex Line is shorted and connected in reverse order, so that the CO_2 flows through the outer tube first and the inner tube second. Usually the valve to this line is closed, but can be opened to achieve an even lower mass flow on the other lines, if needed.
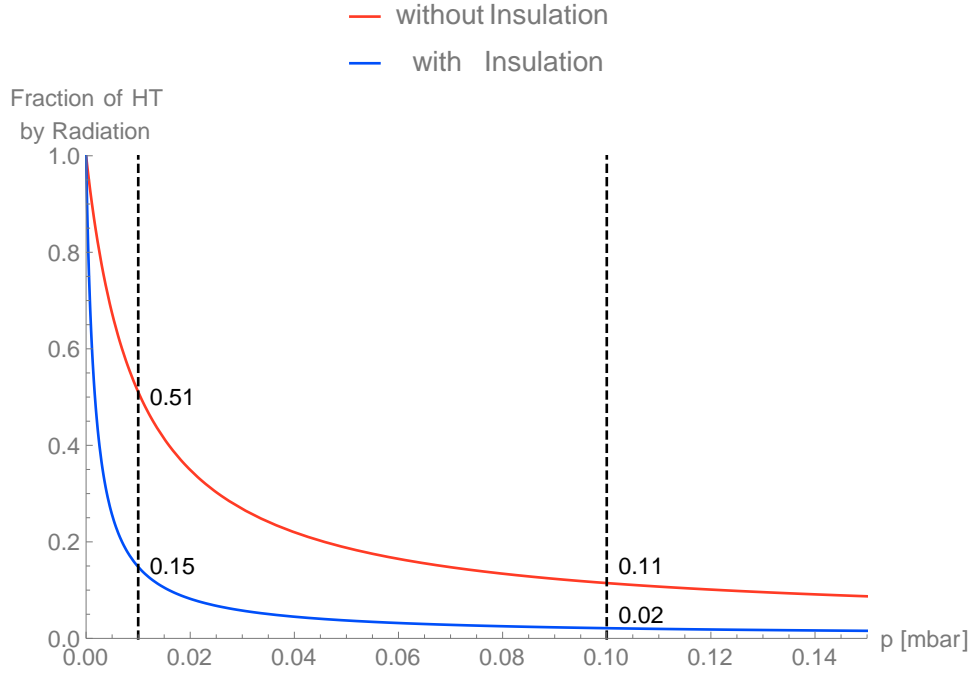
Figure 4.4: Ratio of heat transfer caused by radiation to total heat transfer of an ideal, straight concentric tube dependent on the pressure (gray body approximation, upper limit).
Inner tube: Outer diameter $d_1 = 4\,$mm, temperature $T_1 = -30\,°$C, emissivity without superinsulation $\varepsilon_{Co} = 0.15$, with superinsulation $\varepsilon_{ins} = 0.02$
Outer tube: Inner diameter $d_2 = 8\,$mm, temperature $T_2 = 25\,°$C, emissivity $\varepsilon_{SST} = 0.2$
Values for emissivity taken from [Ver13]

4.3 VXD Layer 6 Mock-Up

The VXD Layer 6 mock-up is a simplified model. It consists of eight ladders with four rectangular sensor dummies each. A fifth trapezoidal sensor is not emulated. Following the naming scheme provided in chapter 2.2.2, these are named L6.*l.s*, with the ladder number $l \in \{1, \ldots, 8\}$ and sensor number $s \in \{1, \ldots, 4\}$. The three sensor dummies L6.*.2 to L6.*.4 of each ladder are provided with electrical heaters and $10\,$kΩ NTC thermistors next to each other. Fig. 4.5 shows a photo of a single sensor dummy with the electrical heater connected to the power supply and the thermistor ro the temperature read-out.

The NTC thermistors cover a temperature range of $-40\,°$C to $125\,°$C, but due to read-out limitations only temperatures up to approximately $60\,°$C can be measured. The electrical heaters have a resistance of about $13\,\Omega$, whose temperature influence has been determined to be smaller than $0.1\,\Omega$ per $40\,°$C. All three heaters of a ladder were connected in series and to a power supply. To reach a heat dissipation of the desired $100\,$W one must apply $0.57\,$A at $7.3\,$V at each heater. To not damage the heaters the voltage should not exceed $7\,$V when uncooled. To not risk such damage the maximum power applied was $(0.55 \pm 0.01)\,$A $\times\ (7.0 \pm 0.1)\,$V $\times\ 24 \simeq (92.4 \pm 1.7)\,$W. To provide better heat transfer from the cooling tube to the heaters and vice versa, a strip of thermally conductive foil is used. To be able to test the cooling tube's influence on the thermistors, different approaches for placing the thermally conductive foil were tried: Putting it straight onto the heater and thermistor (Fig. 4.6(a)), bending it towards the thermistor and away from the tube (Fig. 4.6(b)), and having a separate piece for the thermistor (Fig. 4.6(c)).
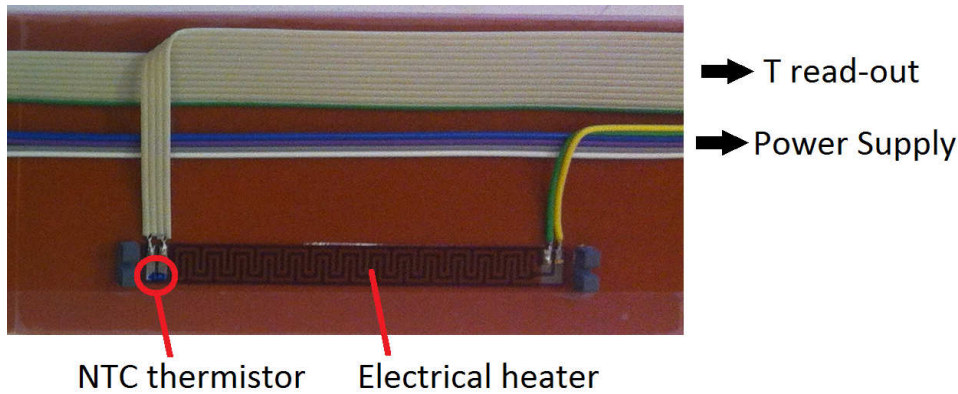
Figure 4.5: Single VXD Layer 6 sensor dummy with NTC thermistor and electrical heater
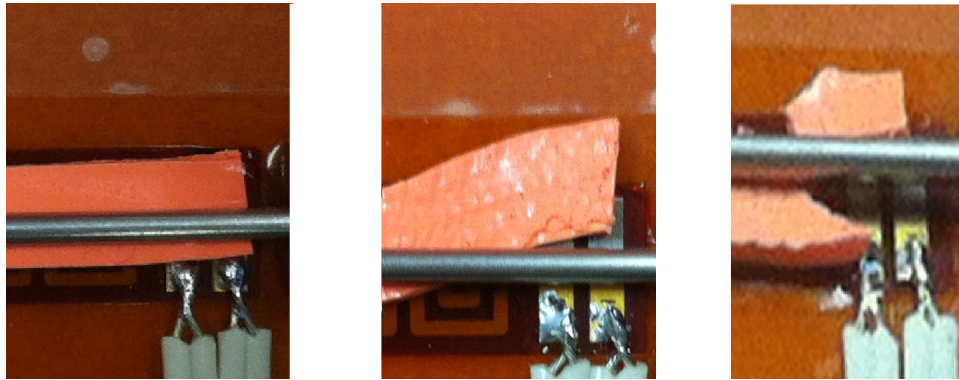
Figure 4.6: Thermally conductive foil placed between heater and cooling tube with different approaches.
From left to right:
(a) Straightly connect tube, heater and thermistor
(b) Bend foil away from tube towards thermistor
(c) Cover thermistor with an own foil

All the ladders were placed next to each other in a flat plane instead of a cylindrical arrangement, like in the real detector. They were slightly slanted, that the cooling pipe could be attached to all of them while having the proper bending radii of 27.8 mm (center of tube). The length of the experiments cooling tube (stainless steel) is 5 500 mm, with an inner diameter of 1.4 mm and outer diameter of 1.6 mm. It is connected to a Flex Line using two 8 000 mm copper tubes, with 3 mm inner and 4 mm outer diameter. The bypasses connections to the Flex Lines and their dimensions are roughly the same as the experiment line's. Their length may vary from 5 500 mm to 6 000 mm.

To gain additional information, four PT100 thermistors were placed at dedicated positions of the experiment. The first two are used to measure the tube's temperature at the experiment's inlet (PT120, Fig. 4.7(a)) and outlet (PT121, Fig. 4.7(b)) and the other two to measure heater temperatures. One of these is positioned directly onto the heater covered with a thermally conductive foil (PT122, (Fig. 4.7(c))), probably being influenced a bit by cooling. The other has it's own thermally conductive foil, with a gap to the cooling tube's, connected to the heater. In this case heat transfer from the tube should be avoided. One has to note, that the PT100 were not well calibrated and their deviation from the real temperature was about 0.5 °C. A quick check suggests that they are most sensitive in the center of the sensors, but it is unclear how the measurement is influenced, when only one half of a PT100 is heated or it is not well

attached. Unfortunately, due to this facts, they are not usable for quantitative measurements.
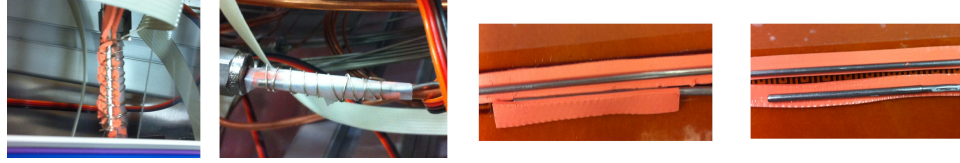
Figure 4.7: Different placements for PT100 used. From left to right:
(a) Experiment inlet, attached to tube (PT120)
(b) Experiment outlet, attached to tube (PT121)
(c) Heater, under thermally conductive foil (PT122)
(d) Heater, onto seperate thermally conductive foil (PT123)

Another approach to get additional information is the usage of a thermal camera placed above the VXD layer 6 mock-up. Different positions were tried: covering the full setup, eight sensors, or four sensors. Having a low resolution of 320×240, the camera only yields clear pictures at the latter position. Some parts of the mock-up, including tubes, thermally conductive foils, and spots on the sensor dummies and heaters, where painted with a thin layer of white color to get rid of reflections on metallic components (such as the tube) and to have points with known emission coefficient of $\varepsilon \simeq 1$.

For this experiment all parts were put in a enclosed chamber and the bypasses were curled underneath the VXD layer 6 mock-up. To reduce their influence on the experiment a solid plastic plate was put in between them. The experiment is superimposed on that plate using nylon screws. Nitrogen is pumped into the volume at a rate of $4\,^\text{L}/_\text{min}$ to avoid condensation or ice on the tubes when operating at temperatures below the dew point of air. Nevertheless sometimes during the operation there were small amounts of ice or water droplets noticed on the tubes. The assembled VXD layer 6 mock-up is shown in Fig. 4.8, ordered by the ladder number with L6.1 in the front to L6.8 in the back.
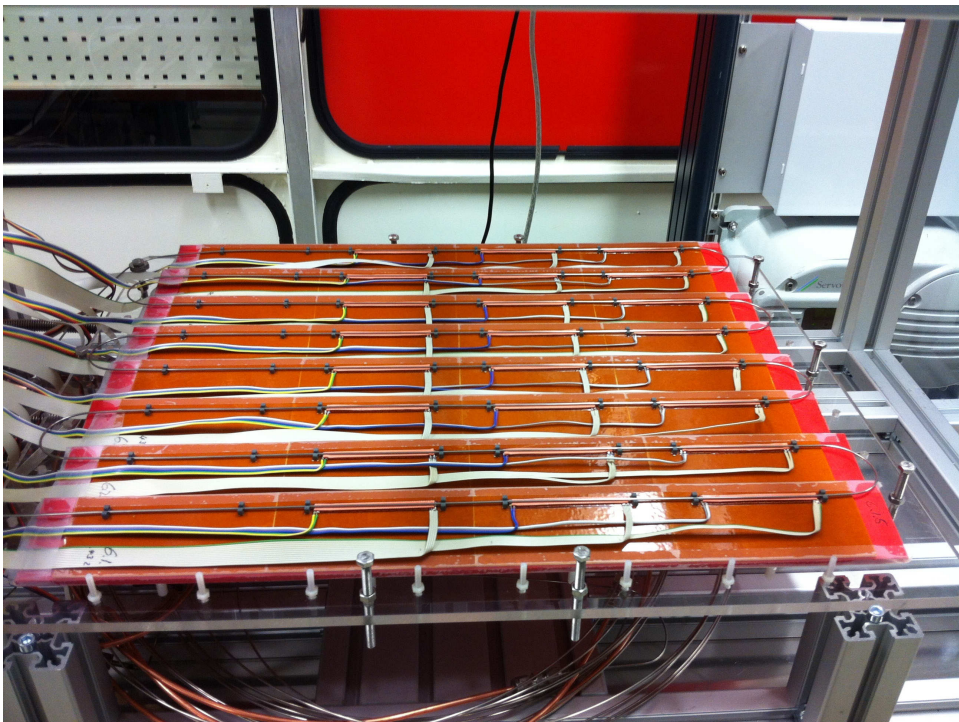
Figure 4.8: Flat arrangement of VXD Layer 6

Experimental Results

Several tests were made using the flat VXD Layer 6 mock-up. Goal of the measurements was to gather knowledge about evaporative two-phase cooling using CO_2 and it's ability to serve as a coolant for Belle II's SVD. The measurements cover the pressure drop along the tubes, test on the cooling performance, and searches for indications of two-phase and dry-out. This chapter describes the methods used and results obtained.

5.1 Pressure Drop Measurements

The pressure drop measurements should give hints about the temperature gradient of the coolant along the tube. While in two-phase, eqn. 3.3 suggests, that a change in pressure yields in a change of temperature $dP \Leftrightarrow dT$. The pressure drop should be as small as possible, because a constant temperature is targeted. Measurements were made at different coolant temperatures and heat loads. Since MARCO's minimum mass flow rate is $5\,{}^{g}\!/_{s}$, bypasses had to be used additionally to the experiment cooling line. To operate at mass flows of approximately $1\,{}^{g}\!/_{s}$ per line, four bypasses were attached in parallel to the VXD Layer 6 cooling. Instead of the directly measured total mass flow $\dot{M}_{\mathrm{meas}}$ a calculated mass flow $\dot{M}_{\mathrm{calc}}$ will be used. This was done with the pump speed f, assuming a linear correlation between f and the real total mass flow $\dot{M}$ at the operated flow rates. The higher accuracy of the pump speed compared to the flow meter allow for more exact results. See appendix A.1 for a comparison between $\dot{M}_{\mathrm{meas}}$ and $\dot{M}_{\mathrm{calc}}$.

5.1.1 Pressure Drop Of Flex Lines

To get the pressure drop on the experiment only, one has to determine the contribution of the Flex Lines in advance. For this purpose six Flex Lines were connected to MARCO in parallel without further tubes. The mass flow of a single line $\dot{m}$ for a given pressure drop is expected to be the same for each. Therefore it is simply given by the relation

$$\dot{m} = \frac{\dot{M}}{n} \tag{5.1}$$

where n is the quantity of lines. Measurements were performed for $-30\,°\mathrm{C}$, $-20\,°\mathrm{C}$, $0\,°\mathrm{C}$ and $20\,°\mathrm{C}$. Fig. 5.1 shows the results of these measurements compared to each other. When calculating the pressure drop dP_{Exp} for the $5\,500\,\mathrm{mm}$ experiment line, the pressure drop dP_{Flex}, for the Flex Line at given temperature, has to be substracted. For more detailed plots including data points see Appendix A.2. One notes, that at lower flow rates the pressure drop is higher for low CO_2 temperatures while at bigger flow rates this is the case for higher CO_2 temperatures. This could be caused by higher vapor quality

in the tube, due to the increased heat flux at lower coolant temperatures. According to Fourier's Law (eqn. 3.11) $\dot{Q} \propto \Delta T$. At low mass flow rates the evaporative cooling is more dominant, while at high ones the contribution of convective cooling is increasing. The increased amount of gas bubbles inside the tube contribute to the friction and therefore the pressure drop. See chapter 3.3 for how the pressure drop can be calculated in two-phase state. This effect was also noticed in all following measurements.
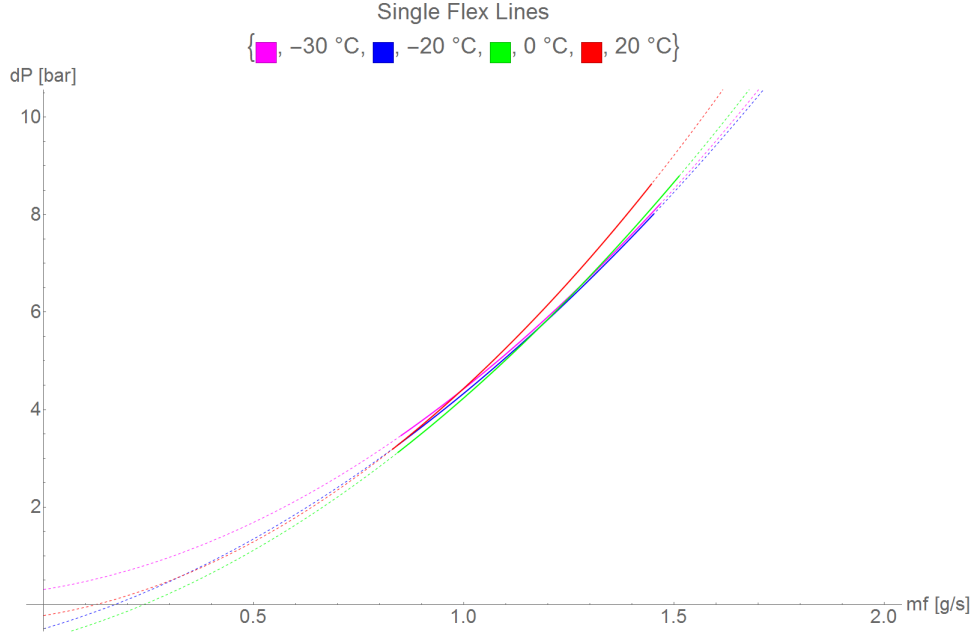
Figure 5.1: Pressure drop for a single Flex Line at different Temperatures. Extrapolated parts are dashed.

A quick test, comparing the pressure drop over a full Flex Line with the inner tubes of the Flex Line only, showed no significant difference. This proves that their contribution is dominated by the inner tubes, which is desired as mentioned in chapter 4.2.

5.1.2 Pressure Drop Of VXD Layer 6

The pressure drop measurements were performed with coolant temperatures of $-30\,°C$ to $20\,°C$, in steps of $10\,°C$. Same thermal powers were applied to the experiment line at all temperatures. Table 5.1 shows the desired and applied power.

Table 5.1: Thermal power applied to VXD Layer 6

Desired Power [W]	Current [A]	Voltage [V]	Power/Ladder [W]	Total Power [W]
0	0	0	0	0
30	0.31 ± 0.01	12.0 ± 0.1	3.7 ± 0.1	29.8 ± 1.0
60	0.44 ± 0.01	17.0 ± 0.1	7.5 ± 0.2	59.8 ± 1.4
92	0.55 ± 0.01	21.0 ± 0.1	11.6 ± 0.2	92.4 ± 1.7

In the case of no power applied, eqn. 5.1 holds for the mass flow through a single unheated line $\dot{m}_{UH}$. If power is applied then the mass flow $\dot{m}_{Exp} = \dot{m}_H$ through the heated experiment line is lower than the mass flow through the unheated ones. The latter can be obtained for a given pressure drop dP_{UH} from

the measurements with the heaters unpowered. Then $\dot{m}_{\mathrm{Exp}}$ can be calculated by refining eqn. 5.1 for a fixed pressure drop to

$$\dot{m}_{\mathrm{Exp}} = \dot{M} - (n - 1)\,\dot{m}_{\mathrm{UH}}$$
$$= \dot{M} - \left(\frac{n-1}{n}\right)\dot{M}_{\mathrm{UH}} \tag{5.2}$$

The pressure drop $\mathrm{d}P_{\mathrm{Exp}}$ over the experiment line only can then be calculated by subtracting the pressure drop over the Flex Line $\mathrm{d}P_{\mathrm{Flex}}$ from the measured pressure drop $\mathrm{d}P_{\mathrm{H}}$ for a given mass flow by

$$\mathrm{d}P_{\mathrm{Exp}} = \mathrm{d}P_{\mathrm{H}} - \mathrm{d}P_{\mathrm{Flex}}. \tag{5.3}$$

Pressure drops for Flex Lines at $-10\,^{\circ}\mathrm{C}$ and $10\,^{\circ}\mathrm{C}$ were interpolated using the average of two adjacent measurements. Fig. 5.2 shows how the calculation of $\mathrm{d}P_{\mathrm{Exp}}$ is performed for $-20\,^{\circ}\mathrm{C}$ and 92 W. Note, that while the errors are small compared to the measured values $\dot{M}$ and $\mathrm{d}P_{\mathrm{H}}$, they come close to 25% of the calculated values of $\dot{m}_{\mathrm{Exp}}$ and $\mathrm{d}P_{\mathrm{Exp}}$.
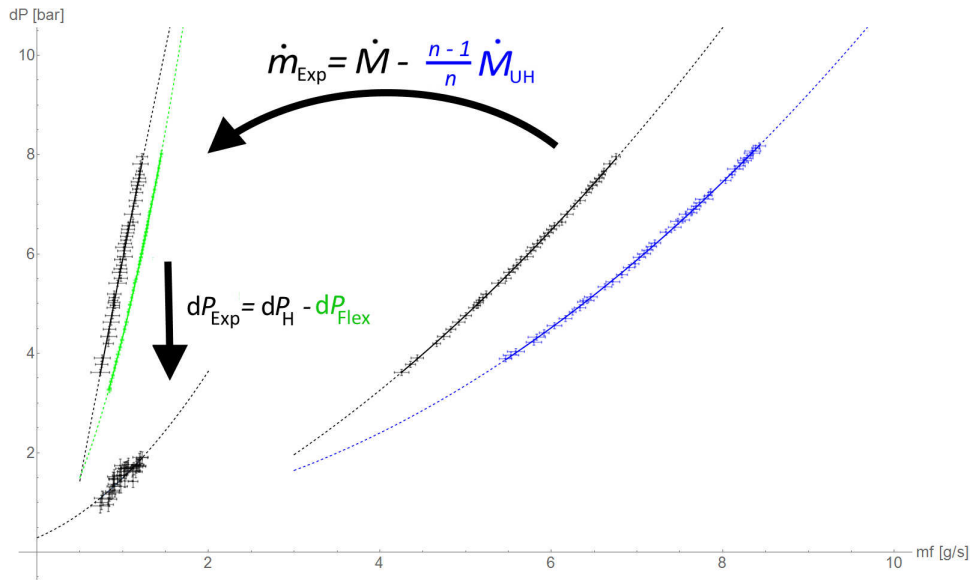
Figure 5.2: Method of calculating $\mathrm{d}P_{\mathrm{Exp}}$ and $\dot{m}_{\mathrm{Exp}}$. Here shown for $-20\,^{\circ}\mathrm{C}$ and 92 W. The blue line indicates the pressure drop $\mathrm{d}P_{\mathrm{UH}}$ for a given total mass flow $\dot{M}_{\mathrm{UH}}$ with 0 W applied (unheated), and the green line the pressure drop $\mathrm{d}P_{\mathrm{Flex}}$ over a single Flex Line with mass flow $\dot{m}_{\mathrm{Flex}}$. The black lines show the progression from the measured total mass flow $\dot{M}$ and pressure drop $\mathrm{d}P_{\mathrm{H}}$ (top right), to the mass flow $\dot{m}_{\mathrm{Exp}}$ and pressure drop $\mathrm{d}P_{\mathrm{Exp}}$ through the experiment line only (bottom left).

The data was taken using a continuous measurement method. The total mass flow was swept from $5\,{}^{\mathrm{g}}/_{\mathrm{s}}$ up to $\approx 8\,{}^{\mathrm{g}}/_{\mathrm{s}}$, until the pressure drop reached about 9.5 bar, to not trigger MARCO's security shutdown. After that the mass flow was reduced to $\approx 4\,{}^{\mathrm{g}}/_{\mathrm{s}}$ and then back to $5\,{}^{\mathrm{g}}/_{\mathrm{s}}$ (as seen in appendix A.1). To get more reliable results, the pressure drops measured from an up going and a down going sweep were averaged. This was done, because the accuracy of the read-out causes steps in the data. This does also mean, that wrong pressure drops were measured for the highest and lowest mass flows, as there is no

data for the reversed sweeping direction there. For this reason the first and last 10% of the data points were cut.

One has to take notice that, due to the large uncertainties, the fitted curves for the experiment line only tend to have a large uncertainty. So some of them seem to have an unnatural curvature. This might also be an issue of the quadratic approximation, which was assumed to be of acceptable accuracy in the measuring range. As an example a comparison of two measurements, of which one is considered to be well represented by a quadratic approximation, while the other is not, is shown in Fig. 5.3 and 5.4. For two out of 24 fits this behavior is conspicuous. However, in the measuring range, one can get an impression of how big the pressure drop is. More detailed plots for every tested combination of coolant temperature and applied power can be found at appendix A.3 to A.14.

A comparison of pressure drops for different heat loads at fixed coolant Temperature shows, that a larger heat load causes higher pressure drops. This is caused by the increasing vapor quality in the two-phase state, which contributes to dP as described in chapter 3.3. See Fig. 5.5 for the comparison at $-20\,°C$.

It was also noticed, that heating caused an higher raise in pressure drop at lower coolant temperatures. At $10\,°C$ the difference of pressure drop is about $\Delta dP_{10\,°C}^{0\,W,92\,W} \simeq 0.6\,bar$ for power of $0\,W$ and $92\,W$, whereas at $-20\,°C$ or $0\,°C$, it is $\Delta dP_{-20\,°C}^{0\,W,92\,W} \simeq 1.3\,bar$ and $\Delta dP_{-30\,°C}^{0\,W,92\,W} \simeq 1.5\,bar$ respectively. This is probably caused by the bigger heat flux through the tube, which is proportional to the temperature difference of the heated outside and the cooled inside according to Fourier's Law. The calculated pressure drop for all tested combinations of dP and T_{CO_2} are enlisted in table 5.2 for Belle II's target mass flow of $1\,g/s$.

Table 5.2: Calculated pressure drop dP at mass flow of $\dot{m}_{Exp} = 1\,g/s$ for given temperature and applied power

T_{CO_2} [°C]	dP [bar]			
	@ 0 W	@ 30 W	@ 60 W	@ 92 W
-30	0.26 ± 0.04	0.89 ± 0.17	1.11 ± 0.13	1.28 ± 0.19
-20	0.26 ± 0.04	0.76 ± 0.25	0.98 ± 0.12	1.23 ± 0.12
-10	0.13 ± 0.04	0.61 ± 0.22	0.81 ± 0.15	1.02 ± 0.20
0	0.20 ± 0.05	0.71 ± 0.20	0.86 ± 0.18	0.93 ± 0.14
10	0.29 ± 0.06	0.55 ± 0.32	0.87 ± 0.26	0.87 ± 0.26
20	0.24 ± 0.03	0.69 ± 0.29	0.86 ± 0.24	0.84 ± 0.12

5.2 Cooling Performance

To test the cooling performance, it was tried to measure the heaters' temperatures for different amounts of power applied, mass flows and coolant temperatures. The measurements were made using the thermistors next to the heaters and the thermal camera. The measured temperatures for different thermistors vary up to $25\,°C$, depending on how the thermally conductive foil was applied (see chap. 4.3). It was also noticed that the temperature differed, if the foil was applied using the same approach. Even small differences in position cause a measurable effect of up to $5\,°C$. Fig.5.6 shows the NTC's readout for a coolant temperature of $-20\,°C$.

The heaters are expected to reach about $70\,°C$ with the maximum applied current and voltage during this test, when uncooled. For this case, the thermistors, which are least directly affected by the cooling pipe by having a separate thermally conductive foil, show a temperature of about $10\,°C$ to $20\,°C$. In
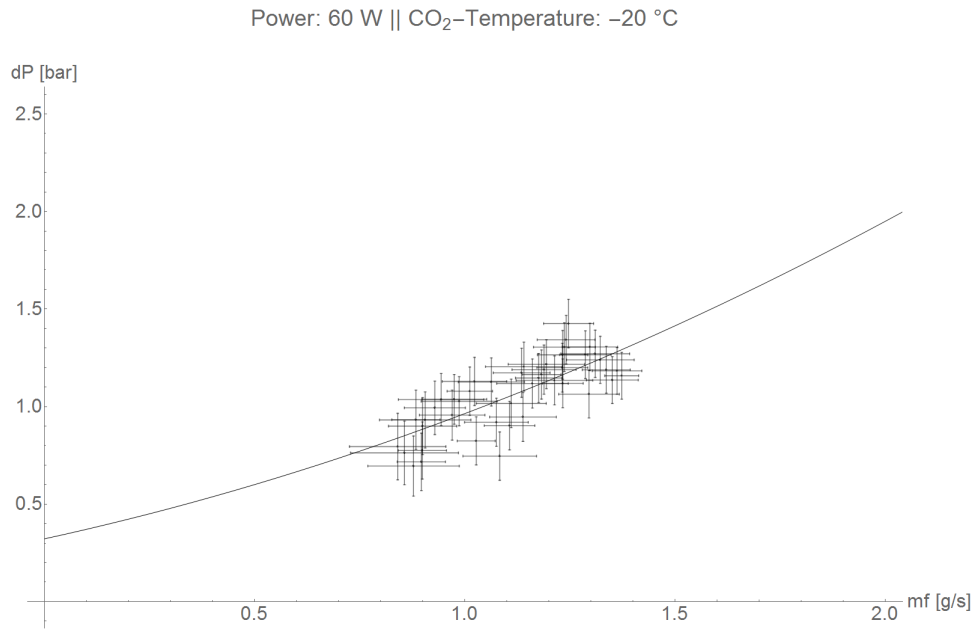
Figure 5.3: Pressure drop over experiment line at 60 W and −20 °C. It is considered to be well approximated by a quadratic function at low mass flows.
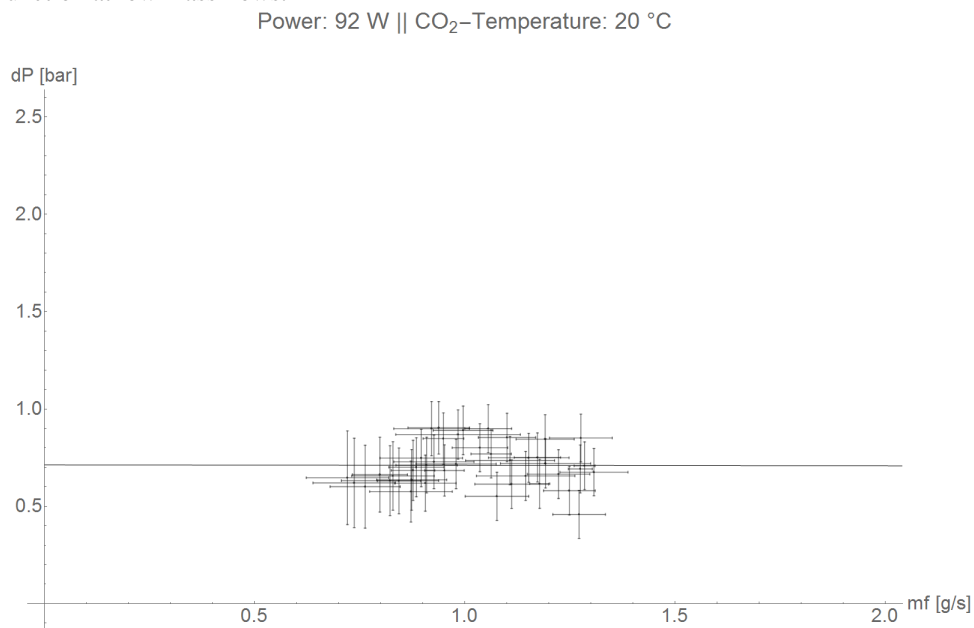
Figure 5.4: Pressure drop over experiment at 92 W and 20 °C. It shows an unnatural curvature (almost none) when trying to approximate with a quadratic function.
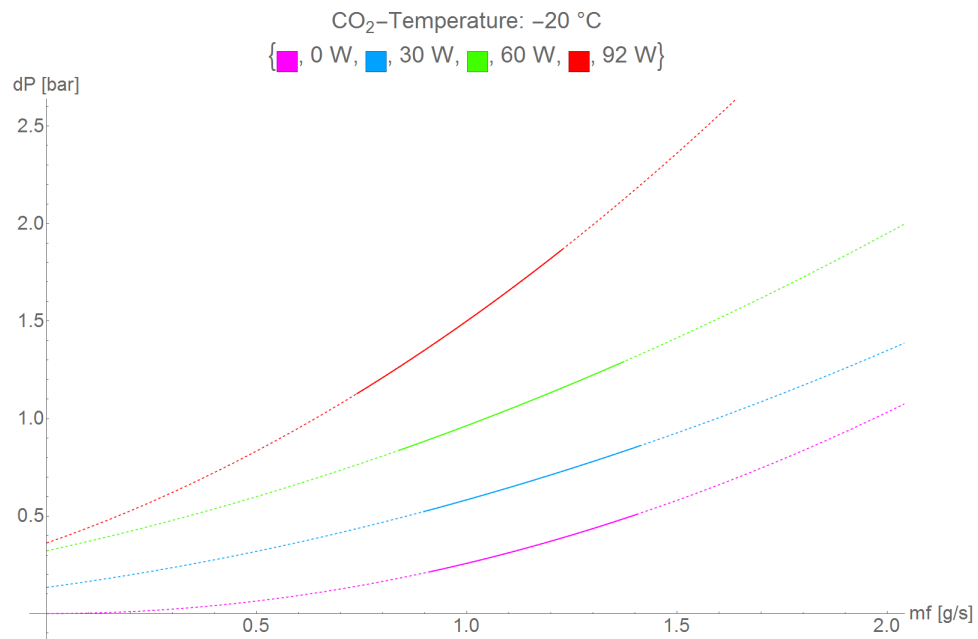
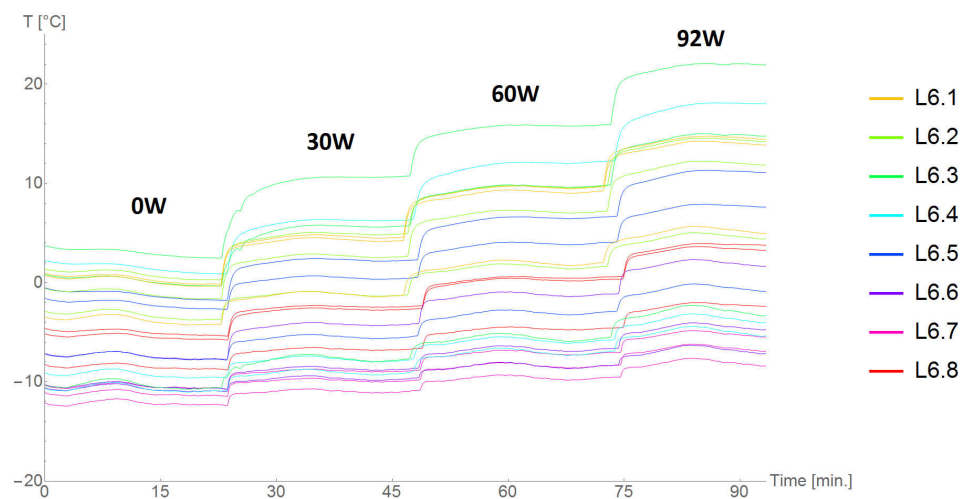Figure 5.5: Comparison of pressure drop for different heat loads at $-20\,°C$. Extrapolated parts are dashed.

Figure 5.6: NTC readout at coolant temperature of $-20\,°C$. Those which are less directly affected by the cooling pipe show a higher temperature.

contrary to this, the thermal camera shows roughly 10 °C more. See Fig. 5.7 for a picture taken at these conditions, showing a view on four heaters. At low coolant temperatures, no differences between those spots which where painted with white color and those without could be seen. At higher ones, clearly visible from 0 °C and above, the cooling tube appeared warmer than the thermally conductive foil. There the white color revealed, that the temperature of the tube was a bit lower. On other surfaces no effects could be observed.
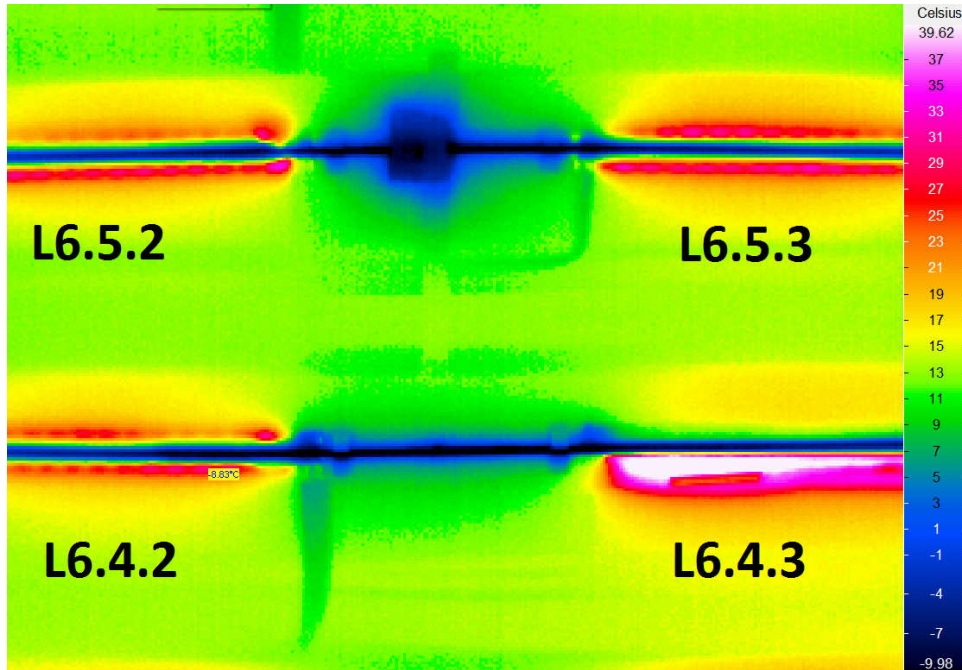
Figure 5.7: Screenshot of thermal camera output at coolant temperature of −20 °C. Detailed view on four heaters. The one on the bottom right has a PT100 attached to it, which has it's own thermally conductive foil, detached from the cooling tube.

Another thing noticed is that at higher flow rates the cooling performance slightly reduces. For low cooling temperatures an incrementation of the total mass flow from $4\,^{g}/_{s}$ to $7.7\,^{g}/_{s}$ leads to a increase in NTC readout temperature of about 1 °C. See Fig. 5.8 for this effect at −20 °C. For higher coolant temperatures this effect is smaller. There might be multiple reasons causing this. Due to the pressure being fixed at the end CO_2 return flow to MARCO, the pressure in front of the experiment line is greater at higher flow rates. This causes the saturation temperature to be above the desired coolant temperature there. Simulations show, that it is likely that the coolant's temperature increases to the saturation temperature fast, as soon as the tube is uninsulated. This causes a lower heat flux from the heaters to the coolant, due to a smaller ΔT. See Fig. 5.9 for a simulation of the experiment line and Flex Lines, showing the pressure and temperature compared to the CO_2 return. As seen there, the pressure drop is expected to cause a temperature drop of the coolant and the tube wall. For this case, the PT100 at the CO_2 inlet tube and outlet tube showed a difference of ≈ 1.5 °C, which is less than the calculated temperature drop of ≈ 3 °C in the simulation. This mismatch could be caused by environment influences and the fact that the PT100 were not calibrated. Additionally to this, it might be, that for the higher mass flows the evaporative cooling is less dominant and therefore the heat flux $\dot{Q}$ through the tube is a bit lower. According to Fourier's Law this is the case, when the heat transmission coefficient decreases. The Thome Model suggests, that the heat transmission coefficient is lower, if

there are low vapor qualities present in the tubes, which is the case for higher mass flows (see eqn. 3.21 and [Tho+08]). Despite to this, Friedel [Fri79] suggests an increasing transmission coefficient via the Dittus-Boelter Equation (3.20), due to the higher mass flow. Both effects could slightly shift the heat flux in different directions. In total these three effects combined could lead to a small decrease of the heat flux. Other unconsidered effects might also have an impact on this.
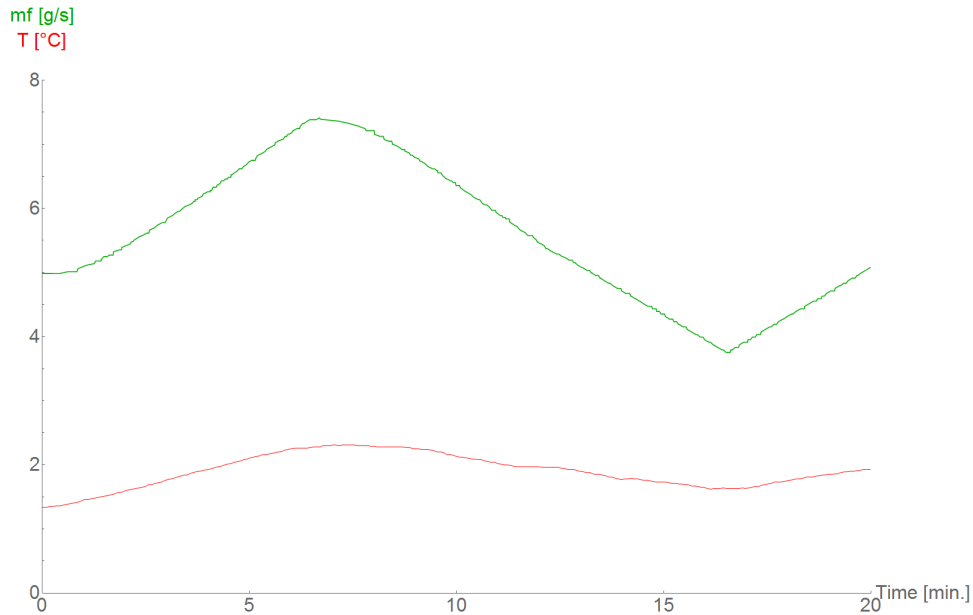
Figure 5.8: Comparison between mass flow (green) and measured temperature (red) at $-20\,°C$ and $92\,W$. One thermistor (L6.6.4) was chosen to keep the curves visible and comparable. Other thermistors show the same behavior. Differences in temperature at same mass flow may be caused by unstable read-out conditions after changing the applied power.

It is unclear how accurate the data is. Both, thermistors and thermal camera, might be inaccurate. For the thermistors, their position could be a reason for the read-out temperature to be lower than the heater's real temperature. To get better results they ought be put onto or beneath the heater. The thermal camera is limited due to it's low resolution of 320×240 pixels. For the distance chosen, where one can see four heaters, this results in a pixel representing a bit less than approximately $1\,mm \times 1\,mm$. Due to the thermally conductive foil, which has a width of $5\,mm$, being slightly smaller than the heater, and the tube covering it's center, the temperature measured with the camera could be a mixture of more and less cooled parts of a heater (Fig. 5.10).

5.3 Indications For Two-Phase

To achieve best cooling performance one has to make sure, that the coolant is in two-phase state, rather than liquid state, as soon as entering the experiment. Usually the cooling unit, in this case MARCO, should provide the right pressure for the saturation temperature to be below the CO_2 temperature, so boiling can occur. Nevertheless the pressure in the system could be slightly higher, because the pressure is set at the MARCO's CO_2 return (see chapter 4.1). Due to the pressure drop being expected to be dominated by the inner Flex Line, the gap to reaching two-phase, if it is not already present, should be small. However, in the current setup there is no way to directly detect whether two-phase is achieved. Tests were performed if one could detect the CO_2's state indirectly by it's cooling behavior. If there
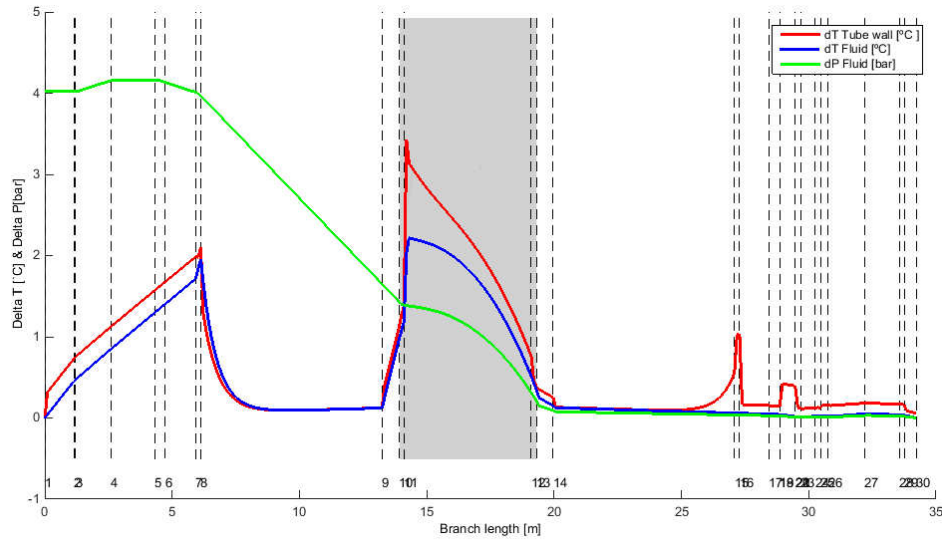
Figure 5.9: Simulation of experiment line with Flex Lines at mass flow $\dot{m} = 1\,\mathrm{g/s}$, temperature set point $T_{\mathrm{sp}} = -20\,°\mathrm{C}$ and a power of $P = 92\,\mathrm{W}$ applied to the experiment. The lines show the difference to the return on the right side in tube temperature (red), coolant temperarute (blue) and pressure (green). The parts shaded in gray are the heated experiment line and it's uninsulated connections to the Flex Line.

Figure 5.10: The thermally conductive foil does not cover the full heater, due to it's smaller width. Measurements might be influenced.

is only liquid in the tube, then the tube's outer temperature is expected to be higher as in two-phase [Ver12]. An increment in applied thermal power should also cause an increase of a liquid coolant's temperature, but in two-phase it should stay almost constant. While increasing the power applied to the heaters of some ladders, the former effect should cause a temperature drop when entering two-phase flow, being measurable at the following NTC thermistors. The latter effect should cause an increment of temperature before that drop, but after that the temperature should be independent from further power raises.

The approach to detect such a phase transition was to slowly increase the applied power at the second ladder. Only tests performed at a set point (saturation temperature) of $20\,°\mathrm{C}$ showed the discussed effects intentionally. This was probably only possible due to the temperature of the CO_2 being harder to control than at lower temperatures. The pumps provide the CO_2 at about $-45\,°\mathrm{C}$ to $-50\,°\mathrm{C}$, which does mean it has to be pre-warmed before the experiment. The higher the requested CO_2 temperature, the more heat intake is needed in front of the experiment using the heat exchanger with the return flow. Even though applying much heat to the return flow, the CO_2's temperature at MARCO's outlet was still a few degrees lower than the saturation temperature, which was not the case at lower set points. Fig. 5.11 shows two possible transitions from liquid state to two-phase. The expected thermal power to reach two-phase in this case was $(13.0 \pm 0.1)\,\mathrm{V} \times (0.53 \pm 0.01)\,\mathrm{A} = (6.9 \pm 0.1)\,\mathrm{W}$. The temperature measured at the first NTC's also increased, because in the Flex Lines there is heat exchange to the inner tube.

33
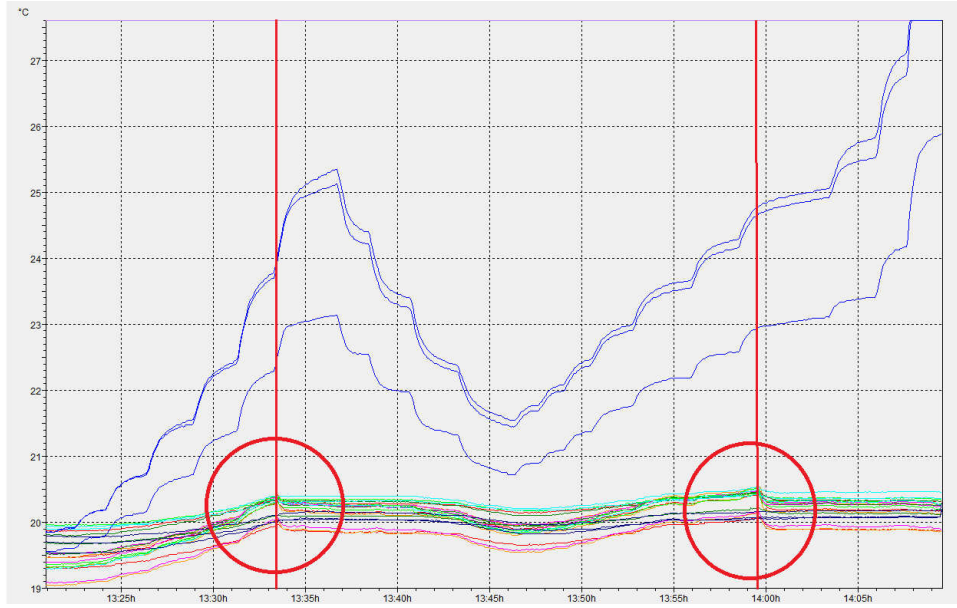
Figure 5.11: NTC read-out at 20 °C. Power was applied to the Ladder L6.2. The blue lines represent their NTC read-out temperature. Other colors show NTC read-out for other Ladders. Possible two-phase entries are marked with red circles/lines.

The same effects as described above occurred unintentionally at lower temperatures, but only when applying heat while MARCO's status was unstable, i.e. after start-up or doing lots of operation. Inducing this at stable statuses was not possible. Due to the measured temperature was not increasing at thermistors behind the heated part, it is assumed that the CO_2 in the experiment's line is in two-phase.

5.4 Dry-Out

The occurrence of dry-out is of interest, because if it would happen in the real Belle II detector, it could cause severe damages to it's components (PXD) or disturb measurements (CDC). The latter is the case for the VXD Layer 6. The worse cooling performance would cause a drastic increase in temperature. Under all circumstances this should be avoided. Attempts were made to provoke dry-out at different heat loads and CO_2 temperatures. Due to evaporative cooling being more dominant at low flow rates, it is expected to reach dry-out easier when operating at the lowest flow possible. Although applying a thermal power of 92 W and reducing the pump speed manually to reach a total mass flow of $\dot{M} = 3.3\,\mathrm{g/s}$ for 5 lines, which corresponds to $\dot{m} < 0.66\,\mathrm{g/s}$, it was not possible to reach dry-out. It was decided to do further testing at CO_2 temperatures of 0 °C and 20 °C. The higher the temperature, the narrower the $P-h$ two-phase parabola, causing dry-out to occur easier than at low temperatures (see chap. 3.1, Fig. 3.1). To further decrease the mass flow on a single line, the fifth bypass was opened causing $\dot{m} < 0.55\,\mathrm{g/s}$. By partially closing the valve to the VXD Layer 6 cooling tube at 0 °C an even lower mass flow was achieved, but it's numerical value got unknown. In this state there might have been an occurrence of dry-out. An indication for this was, that the temperature increased heavily, beginning with the last sensor attached to the cooling pipe and subsequently proceeding to the previous ones. The temperatures gathered by the NTC read-out for this procedure are shown in Fig. 5.12. After reaching these possible dry-outs, the total mass flow was set back to $5\,\mathrm{g/s}$. Otherwise the temperature could have risen more.

For the test done at 20 °C, the heat power was pushed to it's limits of $(24.0 \pm 0.1)\,\mathrm{V} \times (0.62 \pm 0.01)\,\mathrm{A} \times$
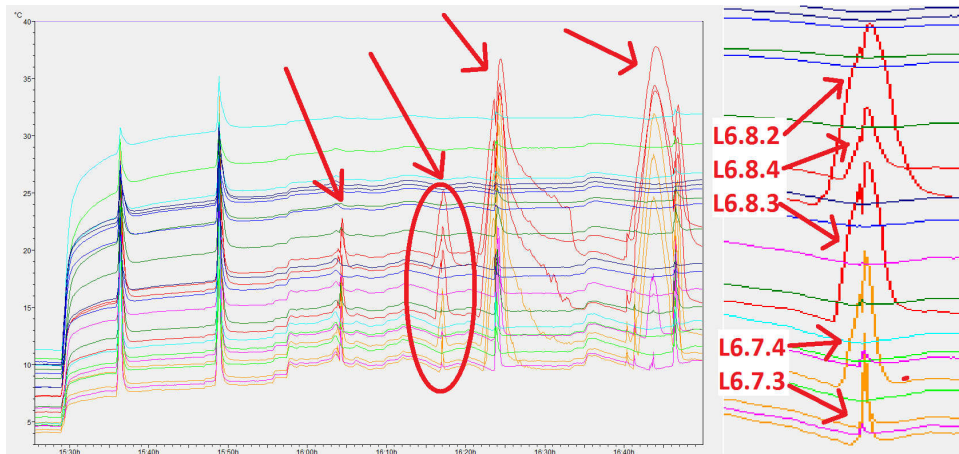
Figure 5.12: Possible dry-outs at 0 °C. The encircled one is shown in more detail to see the order of where temperature rises

8 = (120 ± 2) W and the VXD Layer 6 valve was fully opened again. The total mass flow was decreased to $\dot{M}$ = 1.5 ᵍ/s, meaning that $\dot{m}$ < 0.25 ᵍ/s. This was just enough to lead to a possible dry-out at the end of the experiment line. Only the last two sensors showed an increase in temperature.

The tests indicate, that it is very unlikely to have dry-out in the real detector. The heat intake and the coolant temperature, both, will be lower and the mass flow higher.

Conclusions

In the context of this thesis, tests and measurements with a flat VXD Layer 6 mock-up were performed. It was tried to gain information on it's cooling behavior. To emulate the real Belle II VXD Layer 6, heaters were used to simulate the heat generation of the read-out chips.

Pressure drop measurements show that the main pressure drop occurs in the Flex Line towards the experiment. With increasing power applied to the heaters, the pressure drop over the experiment line also increased. Due to big uncertainties in the calculated values, the achieved results allow for an approximation on how large the pressure drop is, but not for quantitative exact statements. More accurate data will be achieved by the full thermal mock-up, currently under construction at DESY.

The cooling performance could not be tested well. The thermistors did not give reliable information about the heaters temperature. This is mainly caused by their position, being next to the heaters. They might be influenced by the cooling pipe and the environment. Attempts were made to reduce the cooling pipe's influence by different arrangements of the thermally conductive foil. For the thermistors least influenced by the cooling pipe, temperatures of about $10\,°C$ to $20\,°C$ were measured at a coolant temperature of $-20\,°C$ and an applied power of $92\,W$, whereas the uncooled heaters are expected to reach about $70\,°C$. It is unclear how well the measured temperatures represent the heaters' temperature. A check was done, using a thermal camera, but it is limited resolution may lead to wrong values. It showed about $10\,°C$ more than the thermistors. Tests with an improved arrangement of the thermistors must be done. They should be placed onto or beneath the heaters, directly measuring their temperature without being influenced by the cooling pipe or the environment. It is planned to do so for at least some thermistors in the full mock-up. It was noticed, that the cooling performance is slightly better for lower mass flows, due to a lower pressure and therefore saturation temperature in front of the experiment.

The tests indicate, that two-phase flow is probably always present in the experiment line. In the cases where there was presumably no two-phase flow, it was easily achieved by very low amounts of power applied.

To provoke dry-out, a high amount of power must be applied and the mass flow had to be very low. It is unlikely for this to happen in the real detector at the desired mass flow rates.

As final conclusion, the performed tests and measurements give a first impression of the thermal behavior of a SVD Layer in the experiment. However for more accurate data and predictions of how the real, full detector behaves, improvements have to be done.

Appendix
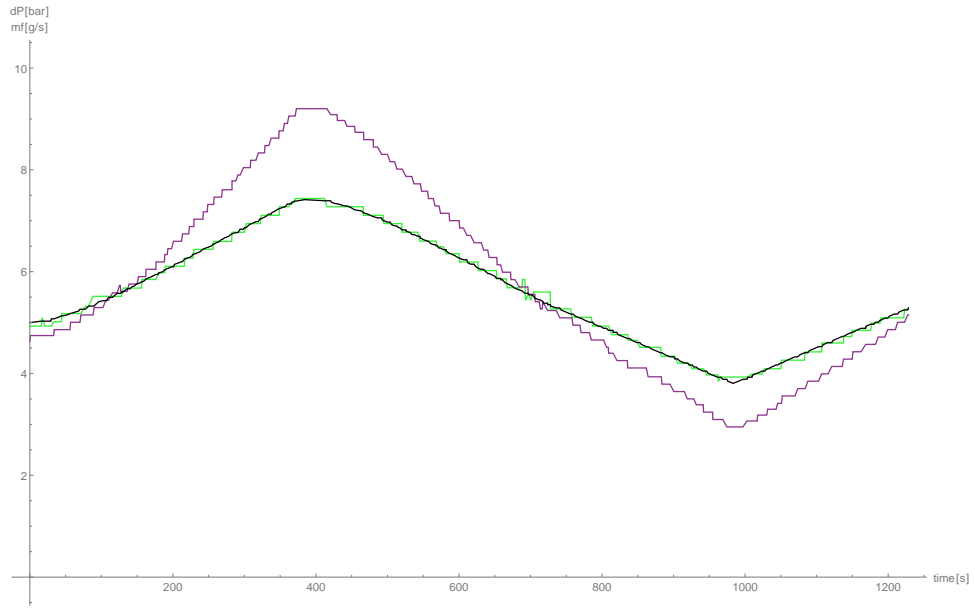
Figure A.1: Plot illustrating the validity of pump speed f to mass flow $\dot{M}$ conversion, assuming a linear correlation $\dot{M} = \dot{M}_{\text{calc}}[\text{g/s}] = \alpha + \beta \cdot f[1/\text{min}]$ in the operated mass flow ranges.
Example: $T(\text{CO}_2) = -20\,°\text{C}$, $P = 60\,\text{W}$. Other parameters yield similar results.
$\alpha = (-20 \pm 2) \times 10^{-2}$
$\beta = (426 \pm 2) \times 10^{-5}$
Shown are pressure drop dP (purpe), measured mass flow $\dot{M}_{\text{meas}}$ (green) and calculated mass flow from the pump speed $\dot{M}_{\text{calc}}$ (black)
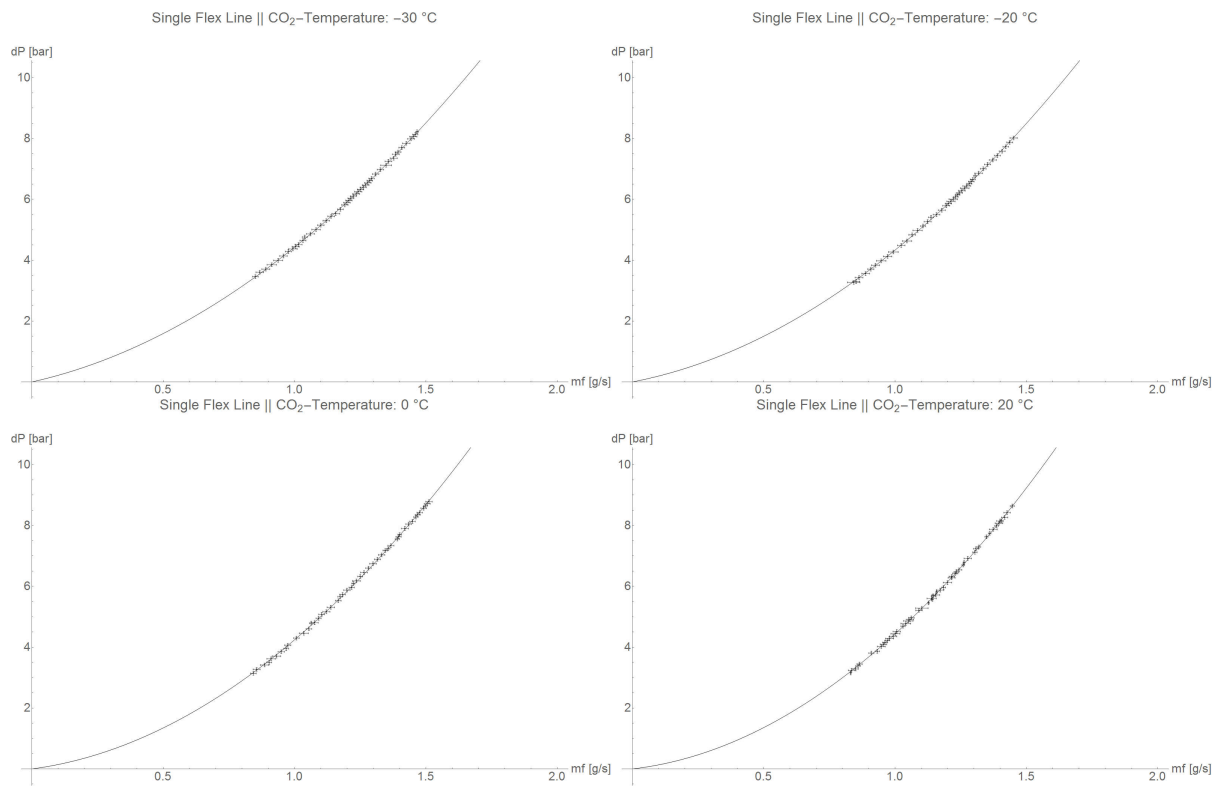
Figure A.2: Pressure drop over single Flex Lines.
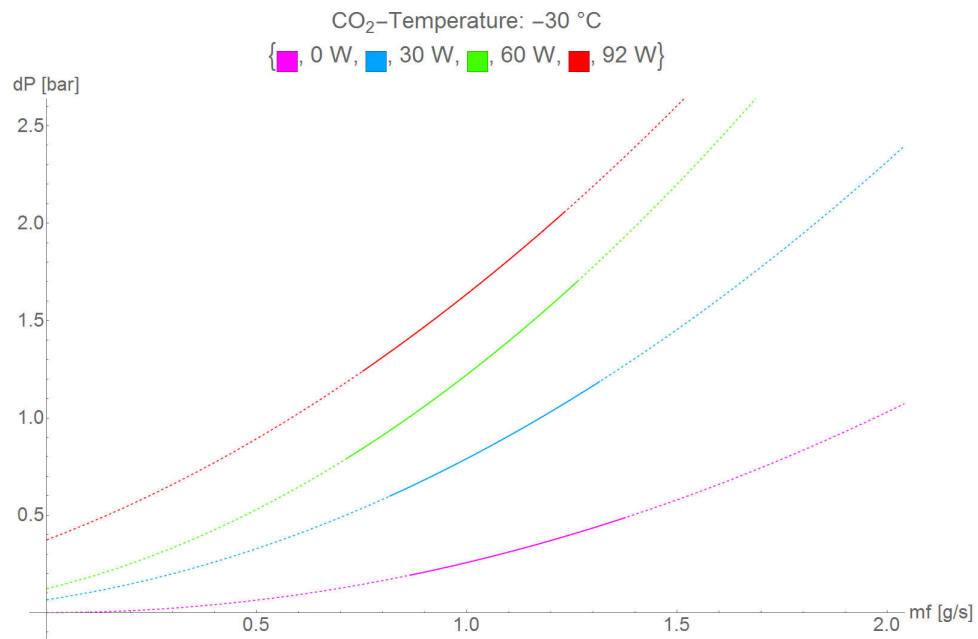
Figure A.3: Comparison of pressure drops at $-30\,°C$ for different powers applied. Dashed parts are extrapolated.
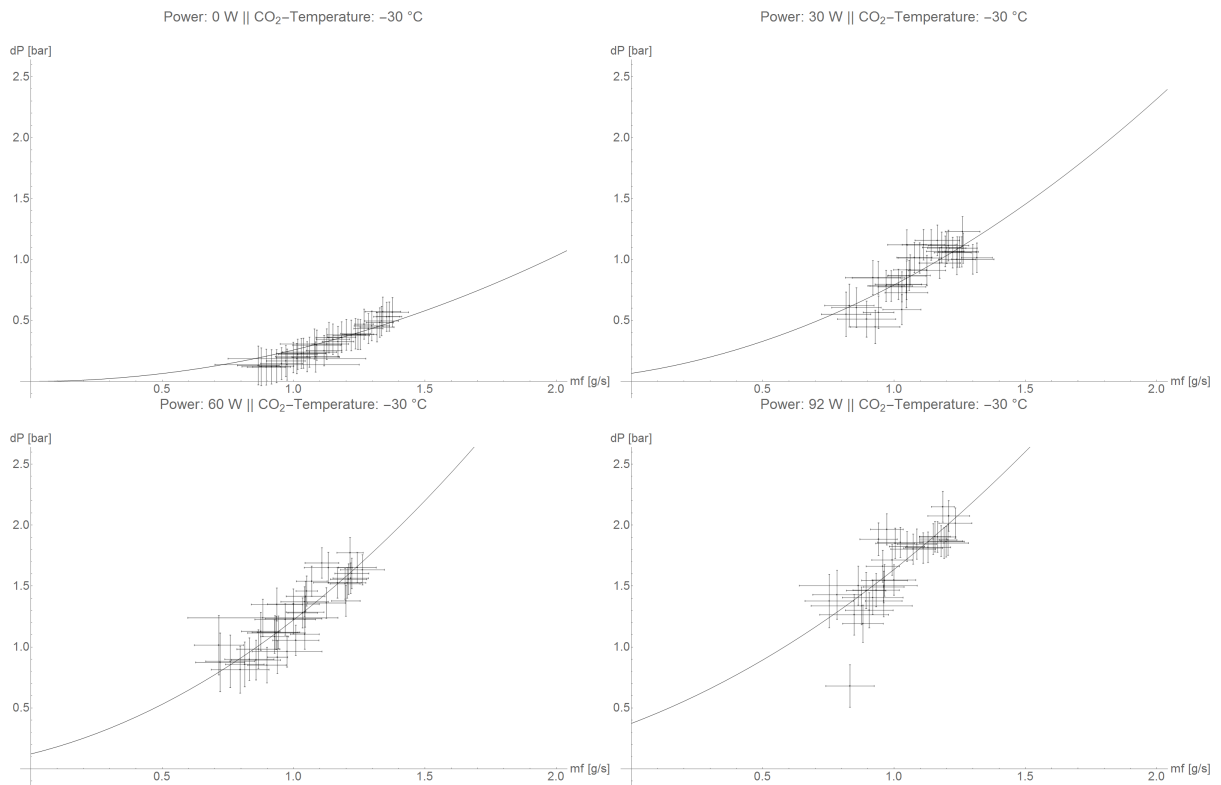
Figure A.4: Pressure drops at $-30\,°C$ for different powers applied.
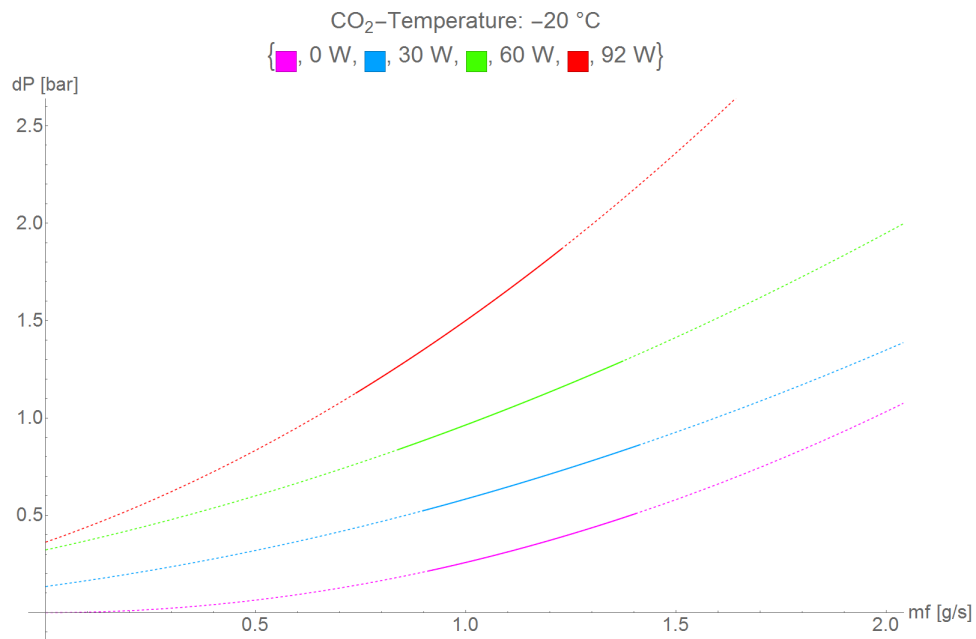
Figure A.5: Comparison of pressure drops at $-20\,°C$ for different powers applied. Dashed parts are extrapolated.
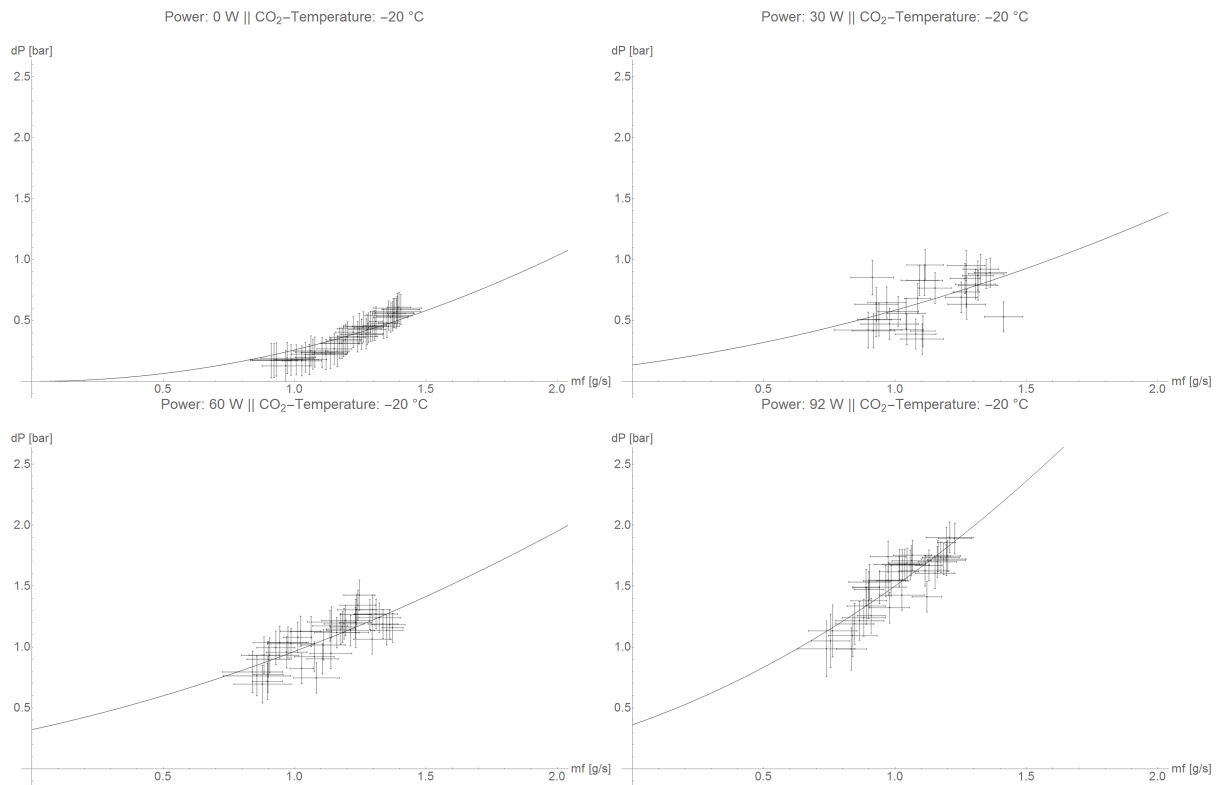
Figure A.6: Pressure drops at $-20\,°C$ for different powers applied.
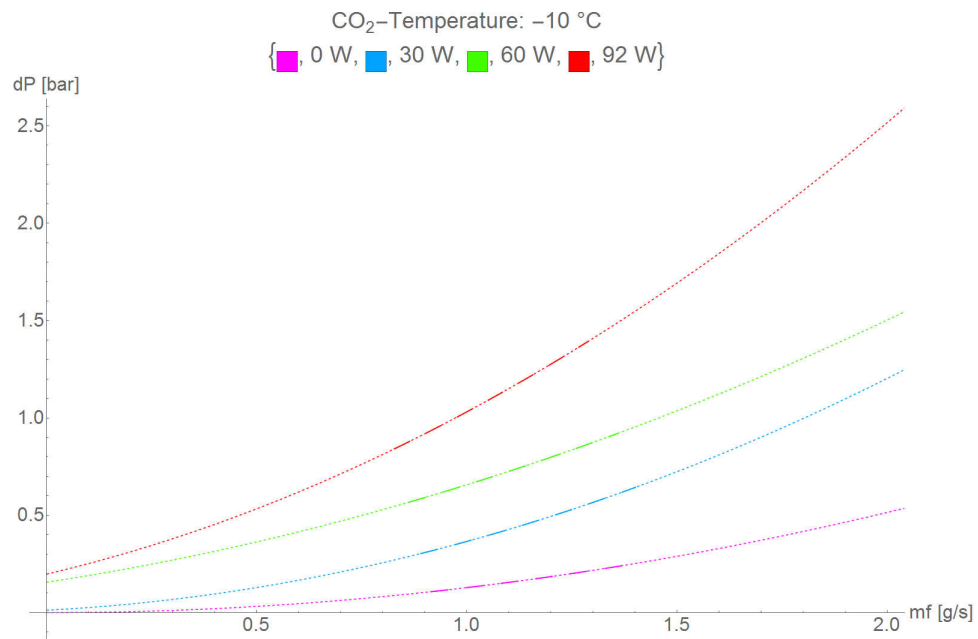
Figure A.7: Comparison of pressure drops at $-10\,°C$ for different powers applied. Flex Line data was interpolated.
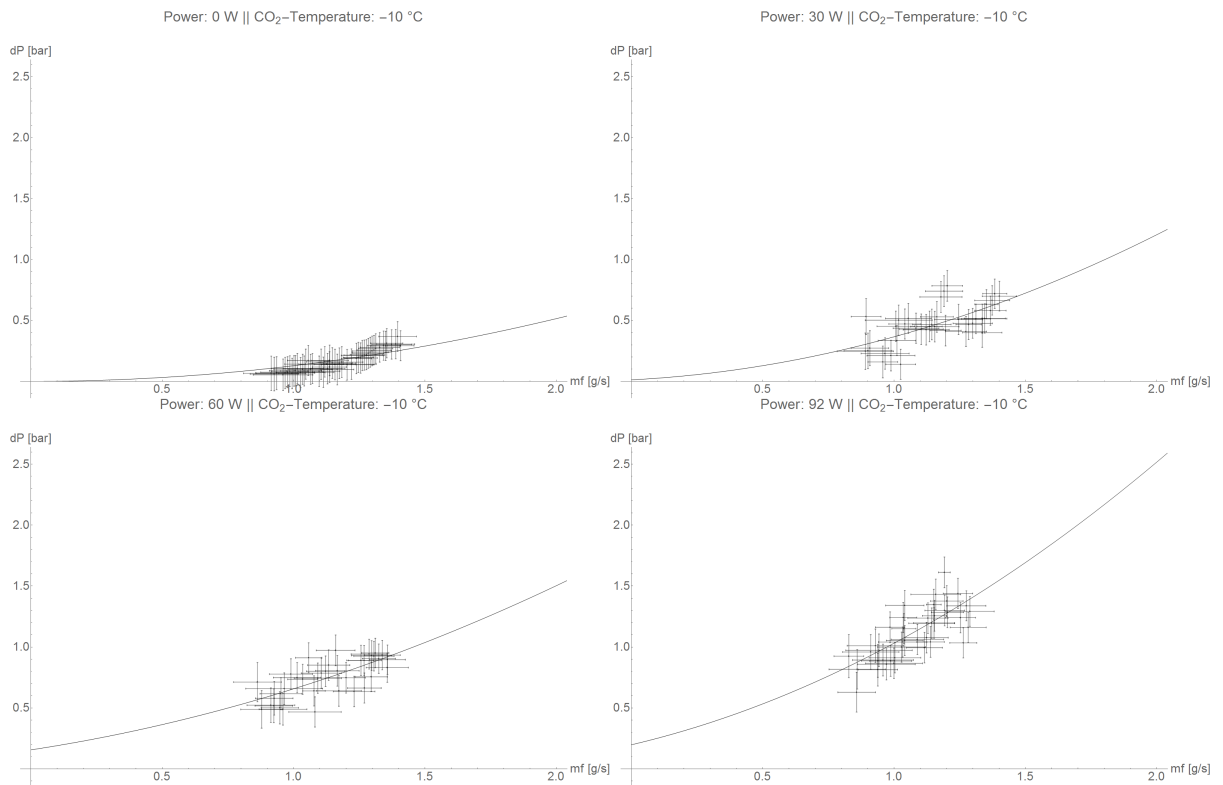
Figure A.8: Pressure drops at $-10\,°C$ for different powers applied.
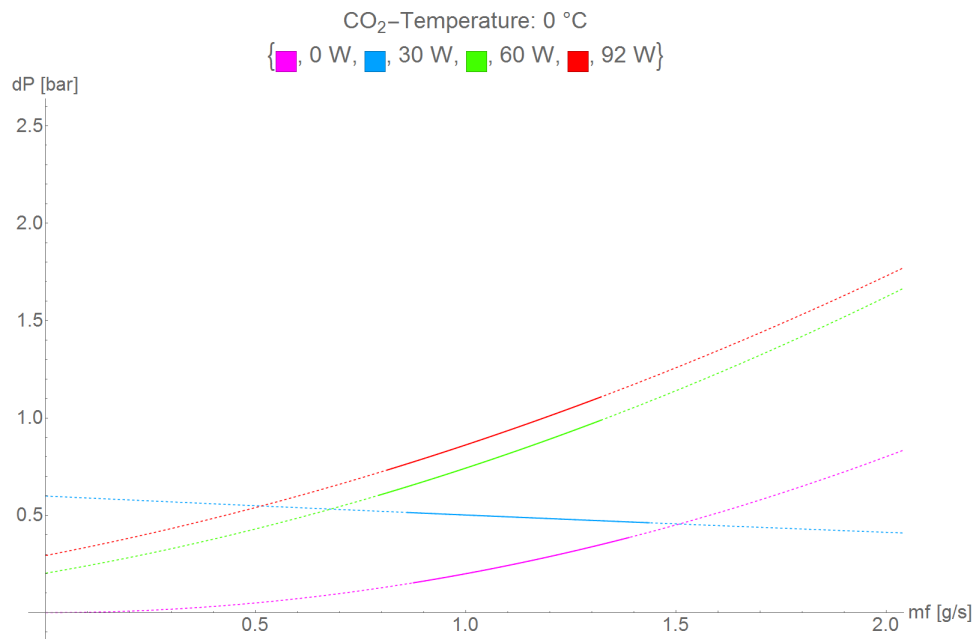
Figure A.9: Comparison of pressure drops at 0 °C for different powers applied. Dashed parts are extrapolated.
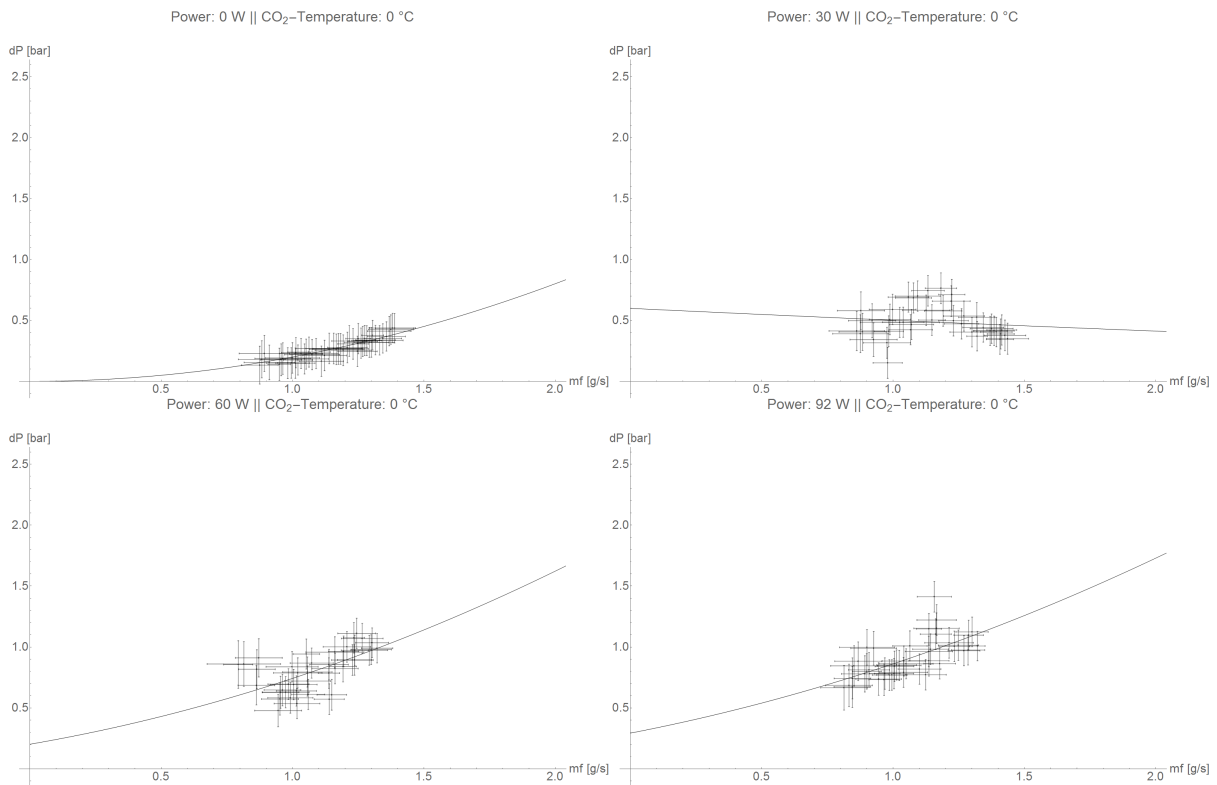
Figure A.10: Pressure drops at 0 °C for different powers applied.
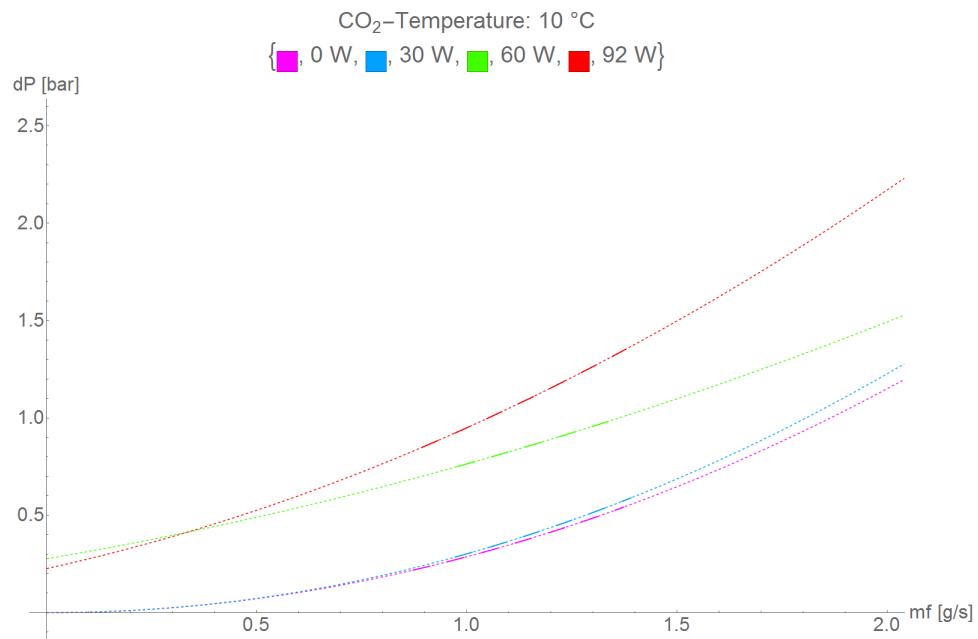
Figure A.11: Comparison of pressure drops at 10 °C for different powers applied. Flex Line data was interpolated.
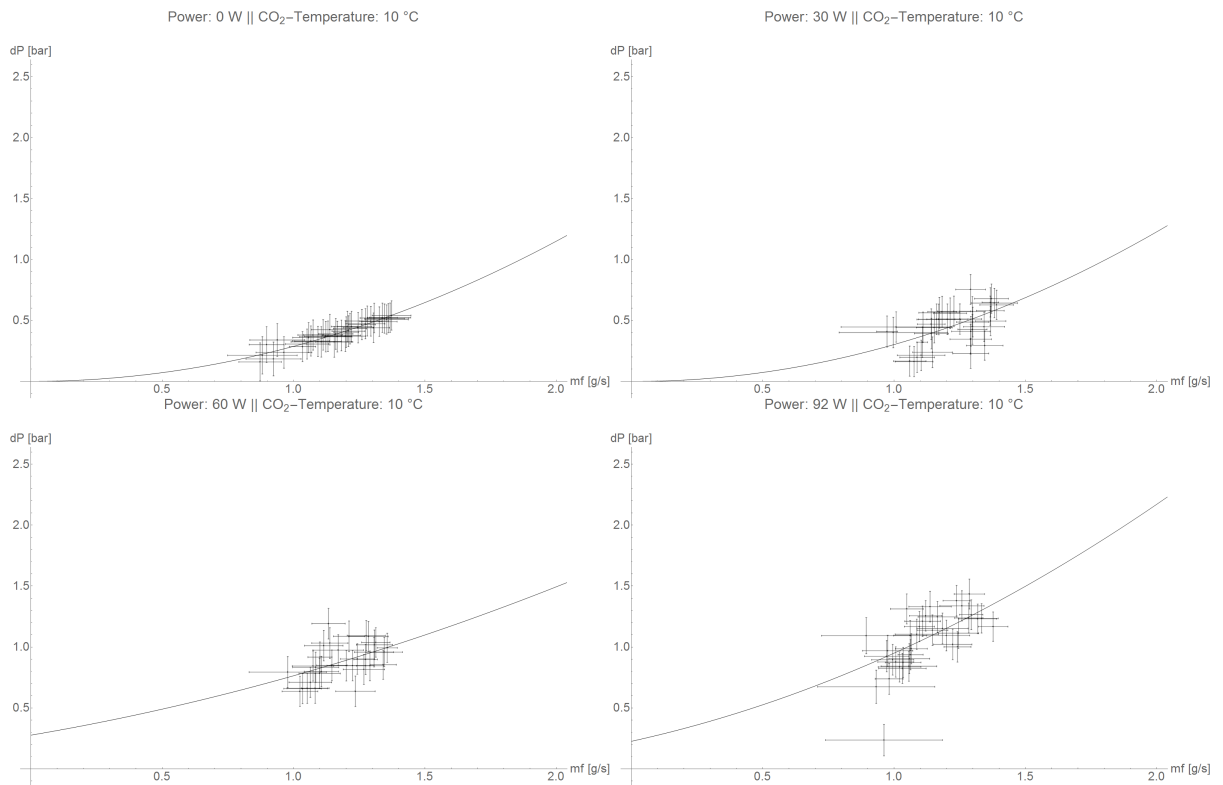
Figure A.12: Pressure drops at 10 °C for different powers applied.
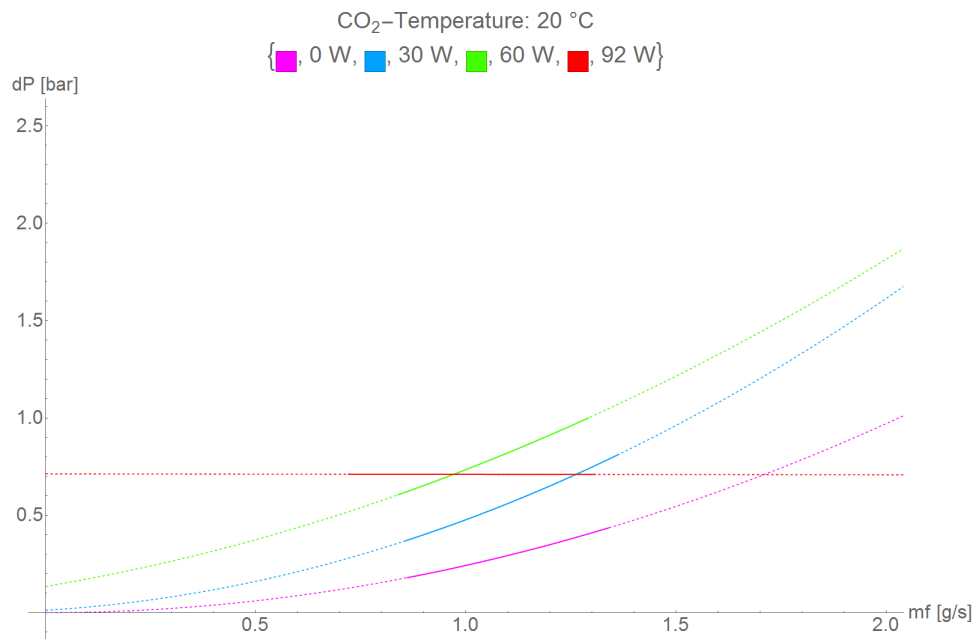
Figure A.13: Comparison of pressure drops at 20 °C for different powers applied. Dashed parts are extrapolated.
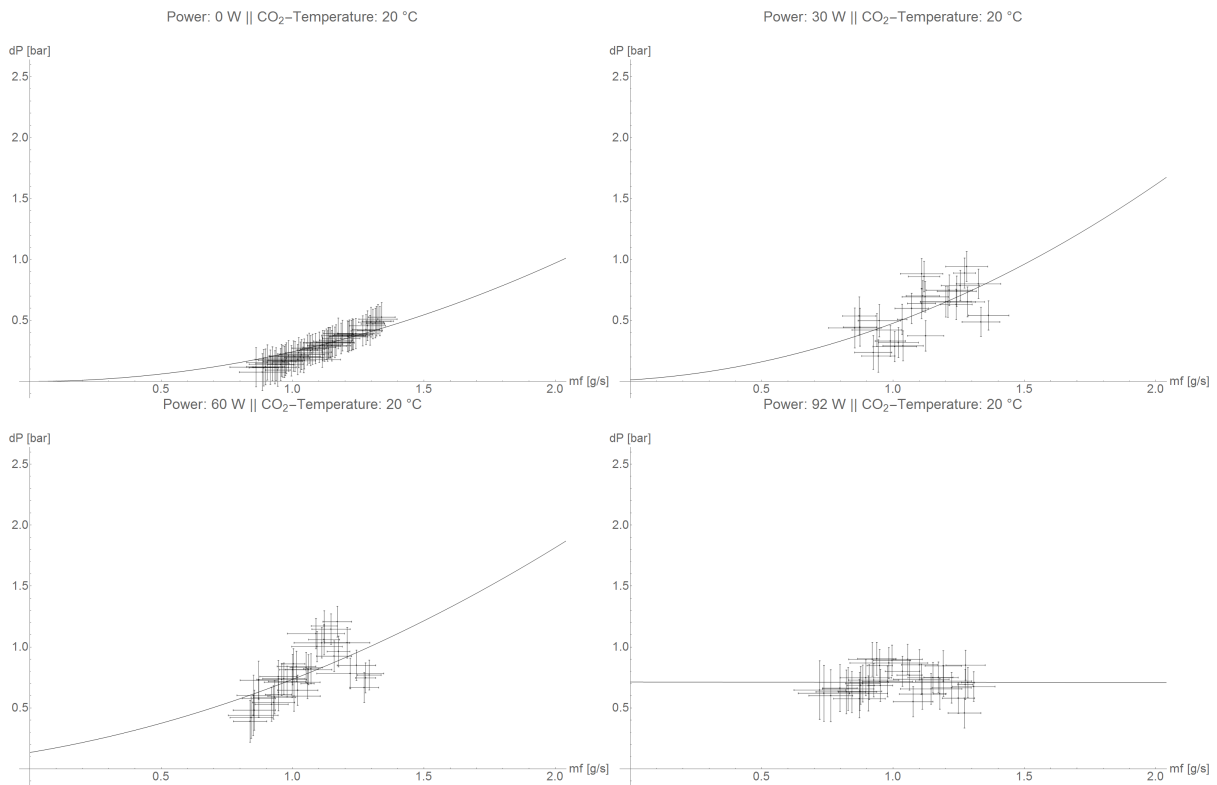
Figure A.14: Pressure drops at 20 °C for different powers applied.

Bibliography

[A+10]   T. Abe, I. Adachi, K. Adamczyk et al., *Belle II Technical Design Report*,
          KEK Report 2010-1, Belle, 2010, arXiv: `1012.1792` (cit. on pp. 1, 3, 4).

[B+12]   W. Bartel, C. Camien, A. Campbell et al., *Belle II at SuperKEKB*, 2012 (cit. on pp. 4, 5).

[Bel]   Belle II / DESY, *Belle II Experiment - Super KEKB and Belle II*,
          URL: `http://belle2.desy.de/e103206/` (visited on 27/02/2015).

[Che99]   Chemica Logic Corporation, *Mollier Chart (Pressure-Enthalpy Diagram)*, 1999,
          URL: `http://www.chemicalogic.com/Documents/co2_mollier_chart_met.pdf`
          (visited on 27/02/2015) (cit. on p. 12).

[Fra13]   A. Frankenberger, *Development of an Open CO2 Cooling System for Belle II* (2013)
          (cit. on p. 7).

[Fri79]   L. Friedel, *Improved Friction Pressure Drop Correlations for Horizontal and Vertical
          Two-Phase Pipe Flow*, European Two-Phase Flow Group Meeting (1979)
          (cit. on pp. 15, 32).

[F+12]   M. Friedl, T. Bergauer, P. Dolejschi et al., *The Belle II Silicon Vertex Detector*,
          Physics Procedia **37** (2012) 867–873, Proceedings of the 2nd International Conference on
          Technology and Instrumentation in Particle Physics (TIPP 2011), ISSN: 1875-3892, URL:
          `http://www.sciencedirect.com/science/article/pii/S1875389212017804`.

[Gfa12]   I. Gfall, *Mechanical Design of the Belle II Silicon Vertex Detector* (2012) (cit. on pp. 6, 8).

[HIG]   HIGH ENERGY ACCELERATOR RESEARCH ORGANIZATION, KEK,
          SuperKEKB Project, URL: `http://www-superkekb.kek.jp/` (visited on 27/02/2015)
          (cit. on p. 4).

[LL62]   L. Lees and C.-Y. Liu,
          Kinetic-Theory Description of Conductive Heat Transfer from a Fine Wire,
          Physics of Fluids (1958-1988) **5** (1962) 1137–1148 (cit. on p. 14).

[M+12]   A. Moll, K. Ackermann, M. Ritter et al., *The vertex detector numbering scheme*,
          Belle II, 2012 (cit. on p. 9).

[Nie14]   C. Niebuhr, *Thermal Mockup Status* (2014), URL: `https:
          //indico.mpp.mpg.de/contributionDisplay.py?contribId=42&confId=2933`
          (cit. on pp. 7, 8).

[Oli+14] K. Olive et al., *Review of Particle Physics*, Chin.Phys. **C38** (2014) 090001 (cit. on p. 3).

[Tho06]   J. R. Thome, *Heat Transfer Engineering Data book III*, Wolverine Tube Inc., 2006
          (cit. on pp. 15, 16).

[Tho+08]   J. R. Thome et al., *New prediction methods for CO2 evaporation inside tubes: Part I - A two-phase flow pattern map and a flow pattern based phenomenological model for two-phase flow frictional pressure drops*,
International Journal of Heat and Mass Transfer **51**.1–2 (2008) 111–124, ISSN: 0017-9310,
URL:
`http://www.sciencedirect.com/science/article/pii/S0017931007002839`
(cit. on pp. 15, 16, 32).

[TCR08]   J. R. Thome, L. Cheng and G. Ribatski,
New prediction methods for CO2 evaporation inside tubes: Part II - An updated general flow boiling heat transfer model based on flow patterns,
International Journal of Heat and Mass Transfer **51**.1–2 (2008) 125–135, ISSN: 0017-9310,
URL:
`http://www.sciencedirect.com/science/article/pii/S0017931007002840`
(cit. on p. 15).

[Ver13]   Verein Deutscher Ingenieure, Gesellschaft Verfahrenstechnik und Chemieingenieurwesen,
VDI-Wärmeatlas : mit 320 Tabellen / Verein Deutscher Ingenieure VDI-Gesellschaft Verfahrenstechnik und Chemieingenieurwesen (GVC)Hrsg. 11., bearb. und erw. Aufl.,
Berlin [u.a.]: Springer Vieweg, 2013, ISBN: 978-3-642-19981-3 (cit. on pp. 14, 16, 19, 20).

[Ver11a]   B. Verlaat, *Conceptual Design Report of MARCO*, EDMS: 1345697 v.1, Nikhef, 2011
(cit. on pp. 17, 18).

[Ver11b]   B. Verlaat, *Controlling a 2-phase CO2 loop using a 2-phase accumulator*,
ICR07-B2-1565, Nikhef, 2011 (cit. on p. 17).

[Ver12]   B. Verlaat, *Evaporative CO2 cooling for thermal control of scientific equipments*,
Nikhef / CERN, 2012 (cit. on p. 33).

List of Figures

List of Tables

Acknowledgements